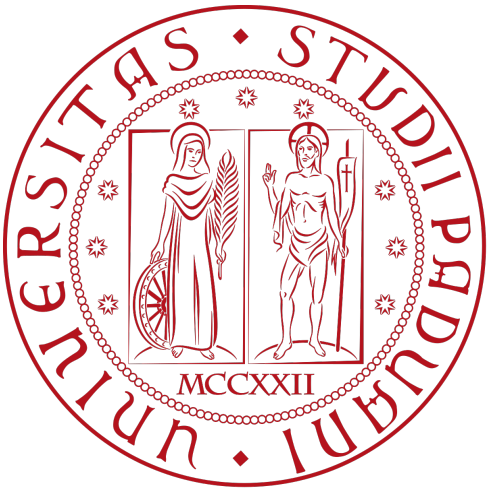

UNIVERSITÀ DEGLI STUDI DI PADOVA

DIPARTIMENTO DI FISICA E ASTRONOMIA

"GALILEO GALILEI"

Corso di Laurea Magistrale in Astronomia

The origin of the Globular Cluster FSR 1758

Relatore:
Prof. Giovanni Carraro

Controrelatore:
Prof. Sergio Ortolani

Laureanda:
Fu-Chi Yeh

Anno accademico 2018/2019

Contents

Listing of figures

Listing of tables

1 Introduction

How the Galaxy formed and evolved has always been an intriguing topic in astronomy. It leads us to understand not only how the universe was formed and evolved on a large scale but is also connected with the formation and evolution of sub-systems such as open/globular clusters and debris of dwarf galaxies at small scale. Through studying kinematic, photometric and spectroscopic properties of these small stellar components, it is possible to understand not only their own evolution history but also how the evolution of the Milky Way influenced them.

Clusters are groups of stars formed together from the same giant molecular clouds and are bound to each other due to strong gravitational attraction. They are categorized into open clusters (OCs) and globular clusters (GCs). Open clusters are young systems consisting of gas, dust and about $10^2 - 10^4$ stars with age mostly below 1 Gyr. Mainly located on the galactic disk, OCs rotate around the Milky Way in nearly circular orbits, and new OCs are still continuously forming from the giant molecular clouds in the disk. On the other hand, GCs are very old (usually more than 10 Gyr) and massive systems, consisting of roughly $10^4 - 10^6$ stars, and with no presence of gas, dust or young stars. They distribute in the halo and the bulge.

Nowadays, the Milky Way contains about 10^5 OCs and 150 GCs. They can be studied as either individual systems within which thousands of stars evolve differently or Galactic subsystems with different populations. Through probing the spatial distribution, kinematic properties, and chemical composition of these systems, the evolution of their surrounding

Galactic environments may become clear. In this thesis, GCs are the main group to be studied. Being one of the oldest systems in the galaxies, GCs witness formation of ancient Galactic halo, bulge and disk/bar, playing an important role in building the Galactic archaeology.

The thesis is organized as follows. Ch.2 is a brief summary of the most important characteristics of the Galactic GCs. The main subject of this thesis, FSR 1758, is focused in Ch.2.7, on the basis of the previous research in which its photometry and spectroscopy were studied carefully. In Ch.3, general procedures of deriving orbits of clusters are introduced and are applied to FSR1758. Results of the orbital calculation are presented in Ch.4 and finally conclusions are made in Ch.5.

The purpose of this thesis is to cast light on the origin of FSR1758 by studying its orbit, and connect it to the characteristics of its photometry and spectroscopy, in order to thoroughly explore its history.

"I look up at the night sky, and I know that, yes, we are part of this Universe, we are in this Universe, but perhaps more important than both of those facts is that the Universe is in us. When I reflect on that fact, I look up—many people feel small, because they're small and the Universe is big, but I feel big, because my atoms came from those stars."

Neil de Grasse Tyson

2

Globular Clusters

The first pioneering step of GCs dates back to 100 years ago, when Shapley (1918) worked on 69 Milky Way GCS and made the first reliable estimate of our distance to the Galactic center dismounting the concept that the Sun is at the center. Though the result was about two times from the present value, later estimates with better data using the same technique led to better estimation of about 8 kpc. From then on, the number of GCs increased over 100 in the mid 20 century and reached 143 in 90s (Djorgovski, 1993). So far, 157 GCs are listed in the catalog by Harris (2010), which is a revision of Harris (1996), but there may be more hidden behind the Galactic bulge. Throughout the century, GCs have been proven to be irreplaceable objects when studying the evolution of stars and clusters as well as galaxy formation/evolution.

In the first part of this chapter (Sects. 2.1-2.6), the up-to-day general knowledge GCs is summarized, including their spatial distribution, appearance, chemical abundance and kinematics. Then in Sect. 2.6, three populations of GCs are briefly introduced by connecting properties in previous subsections, which is crucial when exploring the origin of GCs. Finally, the last part of the chapter Sect.2.7 described the basic characteristics of main subject in the thesis, the GC FSR 1758.

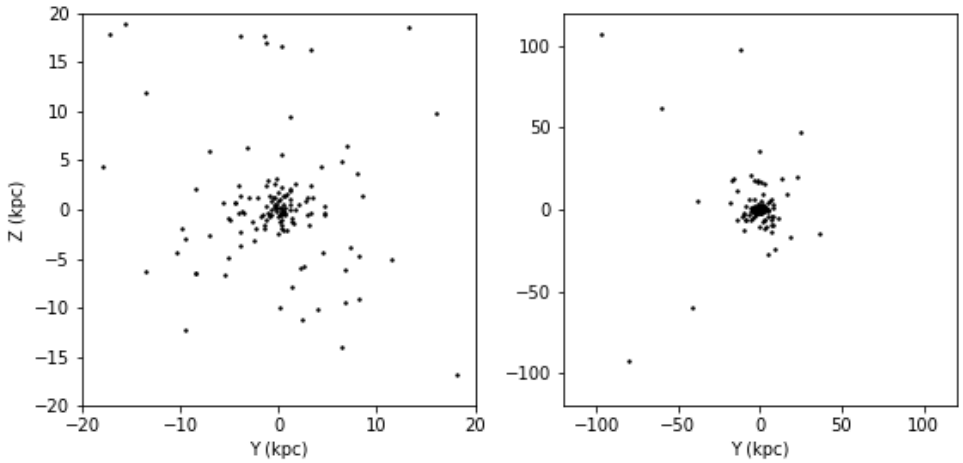

Figure 2.1: Left panel: Spatial distribution of globular clusters in the inner part of the Milky Way, projected onto the Y-Z plane. Here the Sun and Galactic center are at (0, 0) and we are looking along x-axis toward the center. Right panel: Spatial distribution of clusters in the Y-Z plane of the outer region of the Milky Way. The data is extracted from Baumgardt et al. (2019).

2.1 Spatial distribution of GCs

Shapley (1918) first found the Galactic system of clusters distributed spherically towards the center of the Galaxy by utilizing 69 GCs. It is found afterwards that GCs can be divided into different populations based on different spatial distribution (Kinman 1959, Morgan 1959, and Harris 1976). Here, we re-plotted the spatial distribution of 154 GCs with Galactic positions taken from Baumgardt et al. (2019), the most complete collection of proper motions and line-of-sight velocities of GCs to date owing to the latest Gaia data release 2 (Gaia DR2) astrometry (Gaia Collaboration et al., 2018). It's shown in Fig.2.1.

As a result, in respect of distances the distribution of GCs can be divided into two groups. For those within $R_{gc} \approx 40$ kpc, they show a roughly spherical spatial distribution while at distances beyond 40 kpc, the remaining outermost-halo clusters delineate an extended and asymmetric planar distribution that was speculated to have an origin and history outside the Milky Way (e.g., Harris 1976; Zinn 1985). Later on, the spatial distributions of different populations in relationship with kinematics and chemical abundance will be introduced.

2.2 Appearance of GCs

Globular clusters are highly concentrated systems, with $10^4 - 10^6$ stars centered in a few parsec region. The typical stellar density in the center of GCs is $10^4 M_\odot \mathrm{pc}^{-3}$, while the one in the solar neighborhood is $0.1 M_\odot \mathrm{pc}^{-3}$ (Gregersen, 2010). In order to quantitatively describe this spherical and dense structure, King (1962) provided a model in which the appearance of GCs are described by the core radius and tidal radius.

A **core radius** describes the central concentration of GCs by measuring the half surface brightness with respect to the center part; at **tidal radius**, the surface density of GCs drops to zero, at which clusters' stellar densities are indistinguishable from the Galactic background. For a relatively isolated galaxy, its surface brightness profile extends and gradually mixes with the background sky. On the contrary, as a cluster orbits the Galactic center, it experiences tidal forces and gradually get stretched out by these tidal forces. Beyond tidal radius, stars will escape from the cluster potential. In addition, stars evaporate from clusters when they gain enough kinetic energy and get ejected from the cluster entirely. Both situations make the boundary of clusters sharp. With the core radius and tidal radius, it's easier to compare the degree of concentration for different GCs with their concentration which is defined as:

$$c \equiv \log_{10}(r_t/r_c). \tag{2.1}$$

For GCs, the typical value of core radius is r_c = 1 pc, tidal radius r_t = 35 pc, and c ranging from 0.75 to 1.75. The most giant and massive globular cluster in the Milky Way, ω Cen, has r_c = 4 pc and r_t = 70 pc (Sparke and Gallagher, 2007).

2.3 Color Magnitude Diagram of Globular Clusters

It was believed that stars inside clusters formed from the same giant molecular cloud, thus they possess the same age, similar chemical element abundance, and common kinematics. As a consequence, they constitute **Simple Stellar Population**. Because of this feature, GCs have been a good laboratory for testing stellar evolution models. A useful tool to study GCs is the Color-Magnitude Diagram (CMD). It was originated from Hertzsprung-Russell (or H-R) diagram which shows the distribution of stars in terms of luminosity and temperature. CMDs are plotted using observation data in the relationship of magnitude against color. They provide information of ages, chemical abundance, distances, and evolution of clusters as well as stellar evolution of individual stars. Given the color and magnitudes of

members of a GC, its CMD reveals the snapshot of the evolutionary phases of stars with different masses at the same age and composition. Through isochrone fitting of the observed CMD of a GC, its distance, age, and chemical abundance are able to be determined.

Since the ages of GCs are typically tens of billions years, their CMDs have following significant features. First is the **Zero-Age Main Sequence (ZAMS)**. These stars are composed of low-mass stars which are undergoing hydrogen burning in residing cores. On top of the MS stars is the turn-off point **(MSTO)**. At this stage, stars have used up hydrogen fuel in the core and will start to move to the right of the CMD. The age of clusters can be estimated at the turnoff point. After this point, stars move rapidly right across the **Sub-Giant Branch (SGB)** until the **Red-Giant Branch (RGB)** where stars start burning hydrogen in a shell.

As the hydrogen-burning shell gradually moves outward and the inert helium core gradually increases, the red-giant branch (RGB) moves steadily upward. An important feature at this stage for typical GCs is **RGB bump (RGBb)**, where evolution is paused temporarily as H-burning shell crossed the H-abundance discontinuity left by the inner penetration of the outer convection zone.

At the top of RGB locate the brightest stars of GCs, whose helium in the cores are ignited and readjust themselves to a new equilibrium on the **Horizontal Branch (HB)**, where stars have near constant luminosity in different temperatures. If a cluster has higher metallicity or lower age, its HB stars will have larger hydrogen envelopes and lower surface temperatures and will thus be on the red side of the horizontal branch **(RHB)**. But if a cluster is very old, or has low metallicity, or its stars have suffered variable mass loss from their surfaces along the RGB ascent, then the residual hydrogen envelopes will be small, the stars will have high surface temperatures, and the horizontal branch will extend to the blue **(BHB)** side of the CMD. In the middle of HB lies a nearly empty strip where stars are called *variable stars. During this phase stars are not stable and evolve so fast that the probability to find them is small. However, RR Lyrae variables are often found in this strip of GCs.

The last major phase of nuclear burning for GC stars is the **Asymptotic Giant Branch (AGB)** in which two fusion shells– hydrogen to helium and helium to carbon– are burning on top of an inert core. During this phase, stars experience strong stellar winds blowing off their outer layers, leaving central **White Dwarfs (WDs)** in the middle of planetary nebulae. Eventually, WDs become faint and cools down, ending their evolution along the WD cooling line, a sequence almost parallel but about 4 mag fainter than the MS.

2.4 Metallicity of GCs

As mentioned in the last part, stars in the same cluster were thought to form from the same molecular clouds and therefore their chemical abundance, or metallicity, is the same. While stars possess the same characteristics, different clusters have different ages and chemical abundance. This is because when clusters born in the earlier period of the universe, only elements such as hydrogen, helium, or lithium existed from Big Bang nucleosynthesis and therefore the clusters don't have heavy elements which are called metals in astronomy. As stars in these clusters evolved to the late stages of stellar evolution, massive stars suffered great stellar winds and turned into supernovae that blew out their outer layers with metal, enriching the interstellar medium and providing recycling materials for the birth of new stars which constitute clusters with younger ages and higher metallicity. Consequently, from the chemical abundance of clusters, the ages of clusters can be observed.

Quantitatively, the metallicity of a star is defined as the logarithm ratio of the total Iron content of the star with respect to the one of our Sun:

$$[\mathrm{Fe/H}] = \log_{10}(\mathrm{Fe/H})_{\mathrm{star}} - \log_{10}(\mathrm{Fe/H})_{\mathrm{Sun}} \tag{2.2}$$

The ratio can be obtained from the analysis of spectroscopy in which different elements have specific wavelengths of absorption lines. As the development of telescopes advances, it is possible to spatially resolve stars in the clusters and therefore to obtain spectra of individual cluster members. Under this definition, stars with negative metallicity are those with less metal abundance than the Sun, and those with higher metal abundance than the Sun have positive metallicity values. With metallicity values of cluster members, the one for the cluster can therefore be decided by averaging values from its members.

Nevertheless, it is until recent two decades that almost all ancient and massive GCs show **Multiple Stellar Population** (Gratton et al., 2012), which suggests that stars in one cluster in fact formed in different periods of time. With chemical abundances from high resolution spectroscopy, stars show distinctive anomalies in in light elements such as He, C, N, and O as well as Na, Al and in some cases Mg (Gratton et al. (2004) and references therein). The most significant variations are N-C and Na-O anti-correlations. This chemical abundance variation is revealed in the CMDs of clusters, splitting or broadening the MS, SGB and RGB sequences.

While the possible cause of multiple population is still in debate, the most accepted scenario is that when massive stars in the first generation evolved into supernovae, they first re-

moved some of the remaining gas in the cluster. Later on as some stars subsequently evolved into AGB, they blew out stellar winds that were not fast enough to escape the cluster, enriching their host cluster with gas that formed the ingredients of next generations. Therefore, the second generation stars which formed from material polluted by the ejecta of the first generation population show different chemical composition.

2.5 Kinematics of GCs

With strong gravity bound in between each other, members of a cluster share common kinematics, moving together around the galactic center while inside the cluster, stars are free to move about randomly and interact with one another. Observational measurements related to kinematics include **proper motions** in right ascension μ_α and in declination μ_δ, as well as **radial velocities** v_r and the **line-of-sight velocity dispersion** σ_{LOS}.

Proper motions are velocities projected on the celestial sphere and can be obtained from multiple observations. Radial velocities are velocities of stars or clusters toward or away from us. From spectroscopy analysis, radial velocities could be derived from the redshift of blueshift, z, of spectral lines:

$$z = \frac{\lambda - \lambda_0}{\lambda_0} \equiv \frac{\delta\lambda}{\lambda_0} = \left(\frac{1 + \frac{v_r}{c}}{1 - \frac{v_r}{c}}\right)^{1/2} - 1 \approx \frac{v_r}{c} \tag{2.3}$$

The approximation in the last steps holds for $v_r << c$, which is well satisfied for all GCs. Because a cluster as a whole moves in the same relative velocity toward or away from us, its radial velocity is derived by averaging the radial velocities of its members. And the rotational velocity of the cluster can be derived from its radial velocity using the following relation (Armandroff, 1989):

$$v_r = v_{rot} \cos\psi, \tag{2.4}$$

where v_r is the radial velocity with respect to the observer at the Sun and ψ is the angle between v_r, the rotational-velocity vector of the cluster, and the line of sight. σ_{LOS} is the dispersion of radial velocities of each star from the mean radial velocity of the cluster system.

Usually, for stars residing in the galactic disk, they show more rotation then random motion, while stars in the halo move much more randomly with less rotation signatures. This characteristic allows the classification of galactic systems. For instance, Zinn (1985) divided GCs into halo population and bulge/disk population from radial velocities and line of sight

velocity dispersion. Most importantly, because of this property, that different systems exhibit different kinematics behavior, we are able to unveil the mystery of the origin and history of the Milky Way GCs.

2.6 Populations of Galactic Globular Clusters

Studies on different populations of GCs could be traced back to the 1950s, when Kinman (1959) and Morgan (1959) put forward that metal-rich GCs in the Galaxy occupy a relatively small volume of space near the Galactic center, whereas the metal-poor ones spread throughout a much larger volume of the Galactic halo.

This concept got more acceptance and attention when Zinn (1985) linked kinematics of GCs to their metallicity and spatial distribution. He proposed that **metal-poor GCs** with [Fe/H] $<$ -0.8 are found to be distributed spherically throughout the whole volume of the galactic halo and bulge. They possess small rotational velocities (v_{rot} = 50$\pm$ 23 km/s)and large velocity dispersion (σ_{LOS} = 114 km/s). On the other hand, the **metal-rich GCs** with [Fe/H] $>$ -0.8 have a flattened distribution with high rotation velocity (v_{rot} = 152 $\pm$ 29 km/s) and low velocity dispersion (σ_{LOS} = 71 km/s).

While it is clear in sorting metal-poor GCs into a halo or a bulge one, there were different opinions about the metal-rich GCs located near the center. Some studies related metal-rich GCs to the bulge/bar system (Frenk and White, 1982) or thick-disk system(Zinn 1985 and Armandroff 1989). To solve it, Minniti (1996) investigated on the kinematics and metallicity of GCs and field stars at a distance of 1.4-1.8 kpc from the Galactic center, providing evidence that if bulge formed through dissipative collapse, metal-rich GCs are related with the bulge rather than thick disk. Côté (1999) further strengthened points of view of Minniti (1996) through providing measured radial velocities of GCs that are lacking in the previous literature.

On the other hand, Zinn (1993) further classified halo GCs into **old halo** and **young halo** systems, based on the cluster kinematics and metallicity. He found that the old halo clusters are predominantly in the inner halo while the young halo ones extend to greater radii. In kinematics, the mean rotational velocity of all halo GCs are v_{rot} = 44 $\pm$ 25 km/s with dispersion σ_{LOS} = 113 $\pm$ 12 km/s, in agreement with the general feature of halo stars.

However, if halo GCs are divided into old and young groups, old halo GCs have rotational velocity v_{rot} = 70 $\pm$ 22 km/s with velocity dispersion σ_{LOS} = 0.79 $\pm$ 0.26 km/s and young halo GCs have rotational velocity v_{rot} = -64 $\pm$ 74 km/s with velocity dispersion σ_{LOS} = 149

$\pm$ 24 km/s. Compared with old halo GCs which have prograde rotation and small dispersion, young halo GCs have retrograde rotation and significantly higher dispersion. From the perspective of kinematics, the distribution of old halo GCs should distribute more flattened than the young halo GCs, which was also proved to be the case for $R_{GC} < 15$ kpc.

What's more, in aspect of metallicity, young halo GCs doesn't show the tendency of increasing metallicity towards galactic center which is a fossil signature of ancient halo collapse shown in the old halo population. The metallicity gradient of old halo clusters are: $R_{GC} <$ 6, 6 $< R_{GC} <$ 15 and 15 $< R_{GC} <$ 40 kpc with <[Fe/H]> = -1.44 $\pm$ 0.06, -1.8 $\pm$ 0.07, and -1.93 $\pm$ 0.1, respectively.

It is now accepted that the GCs in the Milky Way are divided into three populations which formed from different mechanisms. The three populations are bulge/bar system, old halo and young halo systems. In the following, their formation process and resulting properties are summarized.

2.6.1 Bulge/Bar and Old halo System

In general, metal-rich globular clusters are confined to a region near the nucleus while metal poor clusters are distributed throughout the whole volume of the galactic halo and become more concentrated towards the bulge with increasing metallicity. This trend came to the assumption that GCs in the bulge/disk and old halo systems formed within the Milky Way. It was proposed that a rapid collapse of the halo occurred in the early history of the Milky Way before the galaxy flattened into a spiral disc. During the collapse, clusters formed isotropic and stars in clusters in the halo evolved and enriched the early Milky Way with heavier elements as they turned supernovae. As time passed by, heavy elements became more towards the center. Therefore when subsequent globular clusters formed close to the galactic center, they are more metal-enriched and thus showing an increased metallicity gradient towards galactic center.

It's worth noting that inside galactic bulge, the old halo, disk and bulge populations mix together spatially. Bica et al. (2016) investigated the origins of GCs in the bulge using distances and metallicity and categorized them into a few groups: true bulge GCs inside (d $<$ 3 kpc) and in the outer shell of the bulge (3 $<$ d $<$ 4.5 kpc), probable halo intruders ([Fe/H] $<$ -1.5), disk intruders([Fe/H] $>$ 1.0). In addition, by using numerical integration, Ortolani et al. (2019) studied on the orbits of Terzan 10 and Djorgovski 1 which are GCs located in the bulge and first identified them as halo intruders in the bulge, with metallicity [Fe/H]$\approx$ -1 (Ortolani et al., 2019), in accordance with the categorization of Bica et al. (2016).

2.6.2 Young Halo System

The other scenario of the origin of our Galaxy halo is through the accretion of satellite systems like dwarf galaxies, proposed by Zinn (1993). Dwarf galaxies could be captured by the Milky Way and then disrupted, leaving streams and self-gravitating GCs in the outer Galaxy halo. The most dramatic evidence for the accretion event in the Galactic halo is the **disrupting Sagittarius (Sgr) dwarf galaxy** , provided by Ibata et al. (1994) who discovered the co-moving stars in the direction of the Galactic Center with notable different radial velocities from those of bulge stars. The stars present an elongated structure towards the plane of the Milky Way, implying that it is undergoing tidal disruption before being absorbed by the Milky Way. The structure is now called Sagittarius Stream. In addition, four globular clusters were found in the vicinity of the stream with similar radial velocities and they are M54 (NGC 6715), Arp 2, Terzan 7 and Terzan 8.

Recently, Forbes and Bridges (2010) inspected on 93 Milky Way GCs and showed a clear track in the age-metallicity relation towards young ages for accreted GCs of Sgr dwarf galaxy, distinct from the in-situ formed GCs which have constant old ages. The tendency towards young ages is in agreement with Zinn (1993) where two populations were classified using kinematics and metallicity. In addition, they increased the number of candidate GCs associated with the Sgr galaxy and they are Terzan 7, Terzan 8, Arp 2, Pal 12, NGC 4147 , NGC 6715, Whiting 1, AM4, ad NGC 5634.

Bypast accretion events have been discovered as well. Belokurov et al. (2018) observed an elongated structure of the inner metal-rich stellar halo in velocity space, therefore named as **Gaia Sausage**. Later on Myeong et al. (2018) analyzed this structure of 91 Milky Way GCs in action space which should be a constant when clusters experience little change in potential. Myeong et al. (2018) identified 8 probable and 2 possible Sausage GCs which are NGC 1851, NGC 1904, NGC 2298, NGC 2808, NGC 5286, NGC 6864, NGC 6779, NGC 7089 plus NGC 362 and NGC 1261. According to Myeong et al. (2019), the remnants of this merger exhibit little or no net angular momentum, correspondent with the assumption of an head-on collision. Other ancient events including **Gaia-Enceladus** (Helmi et al., 2018), **Canis Major** and **Kraken** (Kruijssen et al., 2019), and **Sequoia** (Myeong et al., 2019). They are also associated with several GCs and all of them are still investigated substantially.

2.7 Properties of the Globular Cluster FSR 1758

Centered at equatorial coordinates α = 17 : 31 : 12, δ = -39 : 48 : 30 (J2000) and Galactic coordinates l = 349.217°, b = −3.292°, [FSR2007] 1758 (in short FSR 1758) lies behind the galactic bulge and was confirmed to be a globular cluster only recently. It was believed to be an open cluster by Froebrich et al. (2007) who first found the cluster using star density maps obtained from Two-Micron All-Sky Survey (2MASS).

In 2018, Gaia mission (Gaia Collaboration et al., 2018) revolutionized the observation in the Milky Way with the release of precision measurements in astrometry, including positions and proper motions at the sub-milliarcsecond level. Later on, Cantat-Gaudin et al. (2018) confirmed FSR 1758 to be a GC by using Gaia data from the significant difference of proper motions of the cluster from field stars as well as common features of GCs for FSR1758 from Gaia optical CMD. They estimated the Galactocentric distance of the cluster to be 1.6 kpc and the height -0.47 kpc, indicating a position inside the bulge. Hidden in a region of high extinction and reddening, FSR1758 has became one of GCs that arise interests of astrophysicists since then.

Barba et al. (2019) first studied the FSR 1758 carefully by using the combination of optical data from GDR2 and the DECam Plane Survey (DECaPS) (Schlafly et al., 2018), and near-Infrared (near-IR) data from the VISTA Variables in the Vía Láctea Extended Survey (VVVX) (Minniti et al., 2018) which maps the Galactic Bulge and southern disk that are hard to observe due to severe optical extinction. The combination resulted in a more uncontaminated sample of cluster members.

Extracted from Barba et al. (2019), Fig.2.2 shows proper motions, optical CMDs and spatial distribution of cluster members from Gaia Data. Proper motions of cluster members which are centered at (μ_α, μ_δ) = (−2.85, 2.55) mas/yr, are notable from the field stars. Optical CMDs of selected members show clear RGB, RGBp and extended BHB sequences, which also appear in the near-IR CMDs from VVVX survey. In addition, there is no sign of HB clump which shows in metal-rich clusters. This is in agreement with the presence of BHB sequence which mostly emerges in metal-poor clusters. The spatial distribution of the cluster spans 0.3 degree in both α and δ. However, the fitting of the stellar radial density profile from DECaPS data to King's model (King, 1962) obtained a core radius R_c= 0.050 $\pm$ 0.004° (about 10 $\pm$ 1 pc) and a tidal radius R_t = 0.78 $\pm$ 0.22° (about 150 $\pm$ 45 pc), showing the prominent size of the cluster, probably even larger than ω Cen.

What's more, they estimated the distance of the cluster to be 11.5 $\pm$ 1.0 kpc based on:

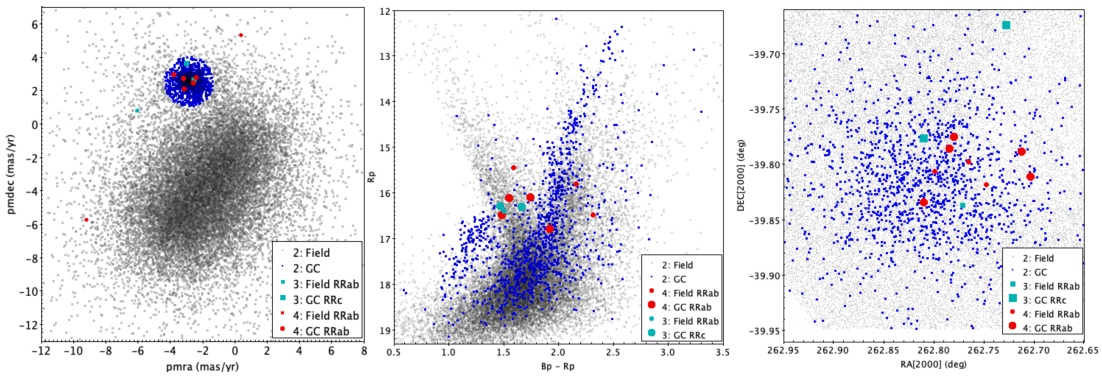

Figure 2.2: Left panel: Gaia proper motions near the cluster region, with the selected members centered at (μ_α, μ_δ) = (−2.85, 2.55) mas/yr marked in blue. Center panel: Gaia CMD of selected stars (in blue dots) compared with field stars in the region (gray dots). Right panel: Spatial distribution of selected members marked in blue. The RR Lyrae variable stars are also shown in red circles for RRab, and cyan for RRc. Large symbols are probable members of the cluster, while small symbols are field stars that belong to the Bulge.

first, the approximated extinction value, and secondly the period-luminosity relation of RR Lyrae variables selected based on the sky positions, PMs, mean magnitudes and positions in the CMDs from OGLE catalog (Soszyński et al., 2014). The estimation of metallicity is derived by comparing its optical and near-IR CMDs to CMDs of two well-known GCs M3 and M13: [Fe/H] = -1.5 $\pm$ 0.3 dex.

In lack of spectra information, radial velocities as well as chemical abundance of stars were missing. However, they were supplemented by the following literatures. In Simpson (2019), five stars have radial velocities measured by the Gaia Radial Velocity Spectrograph (RVS): three of the five stars have 226.5 < v_r < 227.8 km/s, while the other two stars have v_r = −30 km/s and 20 km/s. The three stars with higher v_r are located at the tip of the giant branch of FSR 1758 and are considered to be members of the cluster because of smaller parallaxes than other the two. The averaged radial velocity of the cluster was concluded to be v_r = 227$\pm$ 1 km/s.

It is only recently that Villanova et al. (2019) obtained high dispersion spectra for 9 stars that are confirmed members of the cluster and verified both metallicity of the cluster: [Fe/H] = -1.58 $\pm$ 0.03 dex and the radial velocity v_r = 226.8$\pm$ 1.6 km/s, in accord with values from previous literature. They also found Na-O anti-correlations which are a typical signature of GCs.

"Social relationships among stars are nearly as common as among men and the lower animals. Sidereal bodies completely independent if all star societies are difficult of conception; for the heritage of early and ancestral associations, as well as the immediate environment, influences the present behavior and the density of stars."

Harlow Shapley

3 Orbital Calculation

With the advent of telescopes and satellites, precise positions and velocities of stellar systems become not difficult to acquire and studies on orbits of them enable astrophysicists to understand their history. For GCs, it's difficult to differentiate different populations in the same region. For example, GCs in the bulge can be from the disk or the halo system, and it often takes time to assign them into the right population if using spectroscopy to analyze their chemical abundance. However, if we can derive orbits of interested systems with initial conditions in hand, the assignment work would be faster and the development of constructing the formation history of the Galaxy may become faster.

In this chapter, the general processes to calculate orbits of GCs are present in detail here, including coordinates transformation for the initial conditions (Sec.3.1), the algorithm to solve the equations of motions for clusters (Sec.3.2) and most importantly gravitational potential models utilized in calculating gravitational forces (Sec.3.3).

3.1 Coordinate Transformation

Usually, positions and velocities of stellar objects are expressed in the **Equatorial Coordinate**, which are defined on a sphere centered at the Earth. The sphere is called Celestial Sphere and all the stellar objects are projected onto the sphere. The North and South Celestial Poles (NCP and SCP) are the intersection of celestial sphere with the rotational axis

of Earth. Similar to the longitude and latitude expression used on the surface of Earth, the position of stars projected onto the celestial sphere is expressed by right ascension α (RA) and declination δ (DEC). While DEC has a unit in degree ranging from $-90^{\circ} \sim 90^{\circ}$, RA has a unit in time: hours, minutes and seconds, with a range of 24 hours. The zero-point for RA is called the Vernal Equinox, the location of the sunrise on the first day of spring. The position at $\alpha = 0:0:0$ and $\delta = 0^{\circ}$ is one the intersections of celestial and ecliptic equator. The other one is autumn equinox with α = 12:0:0 and δ = 0°.

With equatorial coordinates, the velocity of a stellar object is obtained by measuring the projection of orbital motion on the celestial sphere within a time duration. The projected motion is split into parallel and perpendicular to the celestial equator, i.e. in the direction of RA and DEC. They are called proper motions, expressed as μ_{α} and μ_{δ} respectively, and the commonly used units are mega-arc-second per year (mas/yr).

Although observational data is usually expressed in equatorial coordinate, for the purpose of galactic research, one needs a coordinate that centers at the Galaxy center, the **Galactocentric Coordinate**. Nonetheless, to obtain the position and velocity in the rest frame of our galaxy, one requires to transform coordinate centered on the Earth to the one centered on the Sun, then from which to the one centered at the center of the Galaxy. The coordinate centered at the Sun is called **Galactic Coordinate**. To do it, we need to rotate the equatorial coordinate to the Galactic coordinate first and then translate the Galactic coordinate to Galactocentric coordinate.

In Galactic Coordinate, the equivalent longitude and latitude are expressed as l and b respectively. The galactic longitude l starts from the line connecting the Sun and the Galactic center, rotating right-handed and ranging from $0^{\circ} \sim 360^{\circ}$. And galactic latitude (b) measures the angle of the object above the galactic plane, ranging from $-90^{\circ} \sim 90^{\circ}$. The North Galactic Pole (NGP) points to the north of the Galaxy, with (α, δ) = (12^{h}:51^{m}:26.275^{s}, +27°:07':41.70").

In Galactic Coordinate, positions of a stellar objects in Cartesian coordinate are usually presented as X, Y, Z. The X-axis points form the Sun towards the Galactic Center, Y-axis points in the direction of Galactic rotation of the Sun and Z-axis directs to the Galactic North Pole. Sometimes people use an opposite direction in X. However, in order to stick to right-handed system with Z pointing upward toward the NGP, we choose the former one.

The coordinates (X, Y, Z) are defined as:

$$X = R\cos b\cos l, Y = R\cos b\sin l, Z = \sin b, \tag{3.1}$$

where (l, b) are the Galactic longitude and latitude, and R is the distance of the object from the Sun. In this coordinate system the Sun is at (0, 0, 0) kpc and the Galactic center is at about (8.2, 0, 0) kpc. The number varies depending on different measuring methods. The velocity components along the X, Y, Z direction are U, V, W respectively. As seen from the NGP, the Milky Way rotates clockwise, in opposite rotational direction from the right-handed system.

The rotational matrix T from equatorial coordinate to the Galactic coordinate can be derived easily by pointing the Vernal Equinox to the Galactic center and NCP to NGP using Eq.3.2. Bovy (2011) derived the matrix thoroughly using spherical trigonometry. It is shown in Eq.3.3:

$$\begin{pmatrix} X \\ Y \\ Z \end{pmatrix} = R \begin{pmatrix} \cos b\cos l \\ \cos b\sin l \\ \sin b \end{pmatrix} = T \cdot \begin{pmatrix} \cos\delta\cos\alpha \\ \cos\delta\sin\alpha \\ \sin\delta \end{pmatrix}, \text{where} \tag{3.2}$$

$$T = \begin{pmatrix} \cos\theta_0 & \sin\theta_0 & 0 \\ \sin\theta_0 & -\cos\theta_0 & 0 \\ 0 & 0 & 1 \end{pmatrix} \begin{pmatrix} -\sin\delta_{NGP} & 0 & +\cos\delta_{NGP} \\ 0 & -1 & 0 \\ +\cos\delta_{NGP} & 0 & +\sin\delta_{NGP} \end{pmatrix} \begin{pmatrix} \cos\alpha_{NGP} & \sin\alpha_{NGP} & 0 \\ \sin\alpha_{NGP} & -\cos\alpha_{NGP} & 0 \\ 0 & 0 & 1 \end{pmatrix} \tag{3.3}$$

Since the velocity U, V, W is the derivative of position X, Y, Z, Bovy (2011) derived the transform matrix by differentiating Eq.3.2:

$$\begin{aligned} \begin{pmatrix} U \\ V \\ W \end{pmatrix} &= T \cdot \frac{d}{dt} \begin{bmatrix} \cos\delta\cos\alpha \\ \cos\delta\sin\alpha \\ \sin\delta \end{bmatrix} \\ &= T \cdot \begin{bmatrix} \cos\delta\cos\alpha\dot{d} - d\dot{\delta}\sin\delta\cos\alpha - d\dot{\alpha}\cos\delta\sin\alpha \\ \cos\delta\sin\alpha\dot{d} - d\dot{\delta}\sin\delta\sin\alpha - d\dot{\alpha}\cos\delta\cos\alpha \\ \dot{d}\sin\delta + d\dot{\delta}\cos\delta \end{bmatrix} \\ &= T \cdot A \cdot \begin{bmatrix} \dot{d} \\ d\dot{\alpha}\cos\delta \\ d\dot{\delta} \end{bmatrix}, \text{where} \end{aligned} \tag{3.4}$$

$$A \equiv \begin{bmatrix} \cos\alpha & \sin\alpha & 0 \\ \sin\alpha & -\cos\alpha & 0 \\ 0 & 0 & -1 \end{bmatrix} \begin{bmatrix} \cos\delta & 0 & -\sin\delta \\ 0 & -1 & 0 \\ -\sin\delta & 0 & -\cos\delta \end{bmatrix}, \tag{3.5}$$

and $\dot{d} = v_r$, $\mu_\alpha = \alpha\cos\delta$ and $\dot{\delta} = \mu_\delta$. Therefore,

$$\begin{bmatrix} U \\ V \\ W \end{bmatrix} = T \cdot A \cdot \begin{bmatrix} v_r \\ \mu_\alpha \\ \mu_\delta \end{bmatrix} \tag{3.6}$$

In Eq.3.6, the units of velocities of V and W are in mas/yr while the unit of radial velocity is in km/s. Therefore, it's convenient to convert all units into the same one and usually km/s is the most common expression for velocity. To do it, the relation 1 arcsec = 1AU/1pc is used and a constant k=4.74047 is multiplied to change units from AU/yr to km/s, with tropical year= 365.242198 days and 1AU=1.49×10^8 km. Finally, we obtain U, V, W in km/s through:

$$\begin{bmatrix} U \\ V \\ W \end{bmatrix} = T \cdot A \cdot \begin{bmatrix} \rho \\ k\mu_\alpha/\pi \\ k\mu_\delta/\pi \end{bmatrix} \tag{3.7}$$

Further processes of deriving σ_U, σ_V, and σ_W in Galactic Coordinate are presented in Johnson and Soderblom (1987) by utilizing uncertainty relation:

$$\sigma^2_{F(x,y,z)} = \left(\frac{\partial F}{\partial x}\right)^2 \sigma_x^2 + \left(\frac{\partial F}{\partial y}\right)^2 \sigma_y^2 + \left(\frac{\partial F}{\partial z}\right)^2 \sigma_z^2 \tag{3.8}$$

Therefore, the errors in U, V, W can be obtained with the relation:

$$\begin{bmatrix} \sigma_U^2 \\ \sigma_V^2 \\ \sigma_W^2 \end{bmatrix} = \mathbf{C} \begin{bmatrix} \sigma_\rho^2 \\ (k/\pi)^2[\sigma_{\mu_\alpha} + (\mu_\alpha\sigma_{pi}/\pi)^2] \\ (k/\pi)^2[\sigma_{\mu_\delta} + (\mu_\delta\sigma_{pi}/\pi)^2] \end{bmatrix} + 2\mu_\alpha\mu_\delta k^2\sigma_\pi^2/\pi^4 \begin{bmatrix} b_{12}\cdot b_{13} \\ b_{22}\cdot b_{23} \\ b_{32}\cdot b_{33} \end{bmatrix} \tag{3.9}$$

Notice that when there is only distance error in-hand, the error of the parallax required in Eq.3.9 is transferred from:

$$\delta d = \delta\frac{1}{p} = \left|\frac{\partial}{\partial p}\frac{1}{p}\right|\delta p = \frac{\delta p}{p^2} \tag{3.10}$$

Finally, to transform Galactic coordinate into Galactocentric coordinate, one only needs to translate the center of coordinate from the Sun to the Galactic center. Recently, Bland-Hawthorn and Gerhard (2016) investigated measurements of the Sun's position and velocity relative to the Galactic center from different tracers, and they concluded a best estimate for the distance of the Sun to the Galactic Center: $R_\odot = 8.2 \pm 0.1$ kpc, solar offset from local disk: $z_\odot = 25 \pm 5$ pc, and Sun's tangential velocity relative to Sgr A*: $V_{g,\odot} = 248 \pm 3$ km/s.

$$(X, Y, Z)_{\text{Galactocentric}} = (X, Y, Z)_{\text{Galactic}} + (X, Y, Z)_\odot, \tag{3.11}$$

$$(U, V, W)_{\text{Galactocentric}} = (U, V, W)_{\text{Galactic}} + (U, V, W)_\odot \tag{3.12}$$

3.2 Orbital Integrator

Given a cluster with initial position x and velocity v at time t moving in the Galaxy, if the gravitational forces acting on the cluster are known, we can use an algorithm to generate a new position and velocity for the next time step, and the algorithm is called an orbital integrator. Literally, an integrator derives new position and velocity by integrating the equations of motions (EoMs) composed of differential equations in velocity and position. By integrating galactic force for a the time step Δt, the velocity difference Δv which the velocity of the system has increased/decreased during the time step is derived; similarly by integrating the velocity for a time step Δt, the disposition Δx which the system has moved during Δt is obtained. So the final position and velocity at next time step, $x(t_0 + \Delta t)$ and $v(t_0 + \Delta t)$ are derived by adding the Δx and Δv to the initial values. This procedure can be seen from Taylor series in which EoMs of the cluster at the next time step, $x(t_0 + \Delta t)$ and $v(t_0 + \Delta t)$, is an expansion of different order derivative:

$$x(t_0 + \Delta t) = \sum_{n=0}^{\infty} \frac{x^{(n)}(t_0)}{n!}(\Delta t)^n = x(t_0) + \boxed{\dot{x}\Delta t + \frac{\ddot{x}}{2!}(\Delta t)^2 + \frac{\dddot{x}}{3!}(\Delta t)^3 + O(\Delta t)}, \tag{3.13}$$

$$v(t_0 + \Delta t) = \sum_{n=0}^{\infty} \frac{v^{(n)}(t_0)}{n!}(\Delta t)^n = v(t_0) + \boxed{\dot{v}\Delta t + \frac{\ddot{v}}{2!}(\Delta t)^2 + \frac{\dddot{v}}{3!}(\Delta t)^3 + O(\Delta t)}. \tag{3.14}$$

In Eq.(3.13), two boxes represent Δx and Δv respectively. Since $\ddot{x} = a$ and $\dot{x} = v$, if considering only the first order in Δt term, Eq.(3.13) can be written as:

$$\begin{aligned} v &= \frac{x(t_0 + \Delta t) - x(t)}{\Delta t_0} + O(\Delta t), \\ a &= \frac{v(t_0 + \Delta t) - v(t)}{\Delta t_0} + O(\Delta t), \end{aligned} \tag{3.15}$$

where $O(\Delta t)$ includes all the higher order terms of Δx and Δv. Therefore, the position and velocity at $t + \Delta t$ turn out to be:

$$\begin{aligned} v(t_0 + \Delta t) &= v(t_0) + a(t)\Delta t \\ x(t_0 + \Delta t) &= x(t_0) + v(t_0)\Delta t \end{aligned} \tag{3.16}$$

Eq.(3.16) is commonly used when we want to derive the position and the velocity of an object in a short period of time, so short that the velocity won't change significantly. The error after a single step is in order of $(\Delta t)^2$. This integrator is called first order **Euler integrator**.

Another integrator used for short period but with higher precision is the second-order **Leapfrog integrator**. It's called leapfrog because position and velocity leap over each other during integration. The position at time step t is decided by the velocity at time $(t - \frac{1}{2}\Delta t)$, and the velocity at time $(t + \frac{1}{2}\Delta t)$ is decided by the acceleration at position $x(t)$, from which the position at the next time step $t + \Delta t$ is derived.

$$v(t_0 + \frac{1}{2}\Delta t) = v(t_0 - \frac{1}{2}\Delta t) + a\Delta t; \tag{3.17}$$

$$x(t_0 + \Delta t) = x(t_0) + v(t_0 + \frac{1}{2}\Delta t)\Delta t. \tag{3.18}$$

However, when calculating orbits of GCs, the integrating time duration is usually longer than millions of years. In this case, if Euler or Leapfrog integrator is used, the small Δt needed for precision requires large amount of computational time. Therefore, to make calculation of differential equations more precise and efficient, many algorithms have been invented. Among them, **Gauss-Radau spacings** improve integration accuracy greatly by considering forces at specific spacings within the entire time step rather than just at the beginning or in the middle as in Euler or Leapfrog does. This method enables larger time steps and therefore reduce large amount of calculation time. In the thesis, Gauss-Radau spacings

of 15th order with errors $(\Delta t)^{16}$ (GR15, Everhart 1985) is employed. And in the next chapter (Ch.4.1), the efficiency of three different algorithms (Euler, Leapfrog and Gauss-Radau spacings) will be compared.

3.3 Potential Models

Once initial conditions and the integrator are specified, the orbit of the cluster can be derived once we know the gravitational forces acting on the cluster. Galactic forces are induced by the gravity between the mass of the cluster itself and the mass density distribution of the Milky Way. Therefore, the cluster feels gravitational potential when sliding inside the Galaxy. Galactic potential can be derived from the mass-density of the Milky Way using Poisson equation:

$$\nabla^2\Phi = 4\pi G\rho, \tag{3.19}$$

and the forces can then be derived from the gradient of galactic potential:

$$\overrightarrow{F} = -\nabla\Phi \tag{3.20}$$

However, under the limitation of observation techniques and data, integral mass distribution of the Milky Way is not achievable. Apart from this, in consideration of the computational speed, simple and analytic forms of galactic density distribution and potential models are therefore used for numerical orbital calculation. Most importantly, they must be easy to compute and be constraint by observational data. In the thesis, three models composed of three time-independent, axisymmetric components are used: a central bulge, a plane disk and the spherical halo. In addition,the time-dependent non-axisymmetric bar potential is also considered to investigate its influence on the orbit.

$$\Phi(r,z) = \Phi_b(R(r,z)) + \Phi_d(r,z) + \Phi_h(R(r,z)) + \Phi_{bar}(x,y,z,t), \tag{3.21}$$

where $R = \sqrt{r^2+z^2}$.

The total mass of each galactic component can be derived from the density distribution:

$$M_b = \int 4\pi R^2 \Phi_b(R) dR, \tag{3.22}$$

$$M_d = \int dz \int 2\pi r \Phi_d(r, z) dr, \tag{3.23}$$

$$M_h = \int 4\pi R^2 \Phi_h(R) dR. \tag{3.24}$$

For these models, they must be constrained by some observational data in order to make sure that the analytic Galactic potential resemble the real galaxy. These constraints are galactic rotational curve, local density and local surface density and they can be derived using the following equations:

$$v_c = \sqrt{r' \frac{d\Phi(r,0)}{dr'}}\Bigg|_{r'=r} \tag{3.25}$$

$$\rho_\odot = \rho_b(r_\odot) + \rho_d(r_\odot) + \rho_h(r_\odot) \tag{3.26}$$

$$\sum_{1.1} = \int_{-1.1kpc}^{1.1kpc} \left[\rho_b(r_\odot, z) + \rho_d(r_\odot, z) + \rho_h(r_\odot, z)\right] dz \tag{3.27}$$

Derived by Holmberg and Flynn (2000) and Holmberg and Flynn (2004), the local density of disk has a value $\rho_\odot = 0.102 \pm 0.010 \mathrm{M}_\odot \mathrm{pc}^{-3}$ using Hipparcos data on a volume-complete sample of A and F stars, and the surface density $\sum_{1.1} = 74 \pm 6 \mathrm{M}_\odot \mathrm{pc}^{-2}$ from K-giant stars at the SGP.

The best-fitted parameters of models are found by searching for the minimum weighted chi-square, which is calculated by dividing the chi square value over the number of data points in each constraint and adding up the results:

$$\chi^2_w = \sum_{i=1}^{3} \left(\frac{1}{N_i} \sum_{j=1}^{N_i} \chi^2_{ij} \right), \text{ with } \chi^2_{ij} = \frac{(\text{modeled} - \text{expected})^2}{\text{expected}} \tag{3.28}$$

Model I.

The first model is a revision of the well-known potential from Allen and Santillan (1991), which is composed of a bulge, a disk and a halo. The potential forms $\Phi_b(R)$ and $\Phi_d(r, z)$ of the bulge and the disk are those proposed by Miyamoto and Nagai (1975), and the halo

inside a sphere of radius R_0 is given by Allen and Martos (1986) :

$$\Phi_b(R) = -\frac{M_b}{\sqrt{R^2 + b_b^2}}, \tag{3.29}$$

$$\Phi_d(r,z) = -\frac{M_d}{\sqrt{r^2 + (a_d + \sqrt{z^2 + b_d^2})^2}}, \tag{3.30}$$

$$\Phi_h(R) = \begin{cases} \frac{M_h}{a_h}\left(\frac{1}{(\gamma-1)} ln\left(\frac{1+(\frac{R}{a_h})^{\gamma-1}}{1+(\frac{\Lambda}{a_h})^{\gamma-1}}\right) - \frac{(\frac{\Lambda}{a_h})^{\gamma-1}}{1+(\frac{\Lambda}{a_h})^{\gamma-1}}\right) & \text{, if } R < \Lambda. \\ \frac{M_h}{R}\frac{(\frac{\Lambda}{a_h})^{\gamma}}{1+(\frac{\Lambda}{a_h})^{\gamma-1}} & \text{, if } R > \Lambda. \end{cases} \tag{3.31}$$

M_b, M_d and M_h represent the total mass of the bulge, disk and the halo. The λ symbol is a cut-off radius to avoid an infinite halo mass.

The corresponding density distribution of each component is:

$$\rho_b(R) = -\frac{M_b}{\sqrt{R^2 + b_b^2}}, \tag{3.32}$$

$$\rho_d(r,z) = -\frac{M_d}{\sqrt{r^2 + (a_d + \sqrt{z^2 + b_d^2})^2}}, \tag{3.33}$$

$$\rho_h(R) = \begin{cases} \frac{M_h}{4\pi a_h}\frac{(\frac{R}{a_h})^{\gamma-1}\left((\frac{R}{a_h})^{\gamma-1}+\gamma\right)}{R^2\left(1+(\frac{R}{a_h})^{\gamma-1}\right)^2} & \text{, if } R < \Lambda, \\ 0 & \text{, otherwise.} \end{cases} \tag{3.34}$$

In this model, the parameters b_b, a_d and a_h control the scales of bulge, disk and halo component. If the scale of each component is increased, the range or boundary of correspondent component will become larger. The value of b_d adjusts the scale height of disk. The scale of height of the Milky Way thin disk is about 300 pc, based on the density of stars at Sun's radius as a function of z from the plane (Gilmore and Reid, 1983). The value of b_d should be near the observation value.

The values of these parameters are listed in the second column, upper panel of Table 3.1.

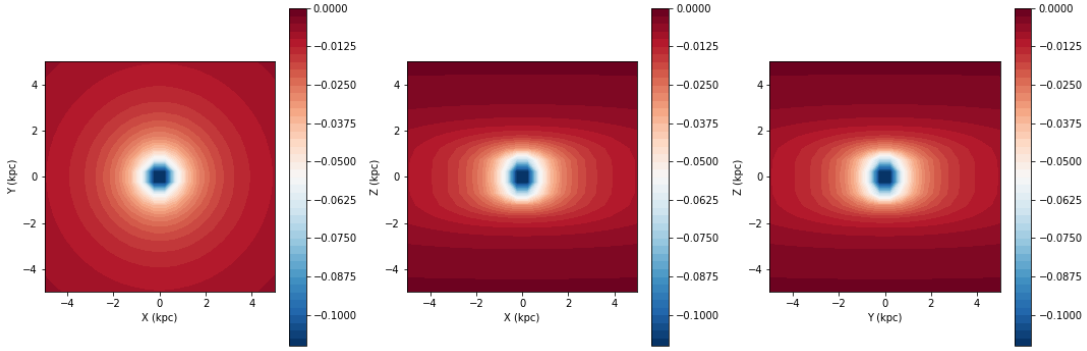

Figure 3.1: Bulge potential with parameters in Moldel I shown in X-Y, X-Z, Y-Z plane. The color bar is in unit of $10^{10} M_{\odot} kpc/Myr$. The size of the bulge is confined in distance smaller than 2 kpc from the Galactic center.

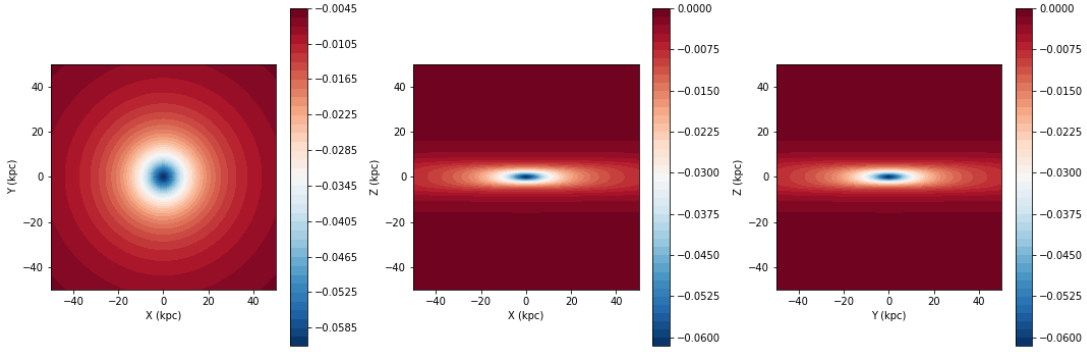

Figure 3.2: Disk potential with parameters in Moldel I shown in X-Y, X-Z, Y-Z plane. The color bar is in unit of $10^{10} M_{\odot} kpc/Myr$.

Parameters	Value*	Best fit	Derived
$M_b(10^{10} M_{\odot})$	0.950925	1.098	1.098
$M_d(10^{10} M_{\odot})$	6.6402	8.9	6.497
$M_h(10^{10} M_{\odot})$	2.36685	2.6657	2.15
b_b(kpc)	0.23	0.27	
a_d(kpc)	4.22	6.22	
b_d(kpc)	0.292	0.33	
a_h(kpc)	2.562	2.39	
χ^2		1.03	

Constraints	Observed	Best Fit
V_r	see Bhattacharjee et al. (2014)	see Fig.3.8
$\rho_{\odot}$	0.102±0.01	0.128
$\sum_{1.1}$	74±6	74.5

Table 3.1: Parameters of Model I. * The values are extracted from Table 1 of Irrgang et al. (2013). The best fit values of parameters are obtained by calculating the minimum χ^2 of constraints.

The constraints: rotational velocities, local density and the surface density, are subsequently derived using Eq.3.25, Eq.3.26 and Eq.3.27 to fit the observation one listed in the lower panel of Tab.3.1. Then search for the minimum chi square value using 3.28 to find the best fitted parameters of models.

Model II

Though the first model was used on many stellar objects successfully, Irrgang et al. (2013) pointed out that because the halo mass of Allen and Martos (1986) is not well constrained by observation, different potential shapes of the halo can yield almost equal matches to the data but differ significantly in other properties. The team used two other halo models form Wilkinson and Evans (1999) and Navarro et al. (1997) to investigate the behavior.

The values of these parameters are listed in the second column, upper panel of Table 3.2. The same procedures to find the best fitted parameters of Model II are used as in Model I.

The halo potential component of Model II. is the one in Wilkinson and Evans (1999):

$$\Phi_h(R) = -\frac{M_h}{a_h} \ln\left(\frac{\sqrt{R^2 + a_h^2}}{R}\right) \tag{3.35}$$

The corresponding density distribution is:

$$\rho_h(R) = \frac{M_h}{4\pi} \frac{a_h^2}{R^2(R^2 + a_h^2)^{3/2}} \tag{3.36}$$

Model III

The halo potential component of Model III. is the one in Navarro et al. (1997):

$$\Phi_h(R) = -\frac{M_h}{R} \ln\left(1 + \frac{R}{a_h}\right) \tag{3.37}$$

The corresponding density distribution is:

$$\rho_h(R) = -\frac{M_h}{R} \ln\left(1 + \frac{R}{a_h}\right) \tag{3.38}$$

The values of these parameters are listed in the second column, upper panel of Table 3.3. The same procedures to find the best fitted parameters of Model III. are used as in Model I.

Parameters	Value*	Best fit	Derived
$M_b(10^{10}M_\odot)$	0.406875	0.3	0.39
$M_d(10^{10}M_\odot)$	6.577425	8.16	7.945
$M_h(10^{10}M_\odot)$	162.110625	160.14	71.865
b_b(kpc)	0.184	0.238	
a_d(kpc)	4.85	5.183	
b_d(kpc)	0.305	0.296	
a_h(kpc)	200	199.14	
χ^2	5.69	1.03	
Constraints	Observed	Best Fit	
V_r	see Bhattacharjee et al. (2014)	see Fig.3.8	
$\rho_\odot$	0.102±0.01	0.129	
$\sum_{1.1}$	74±6	69.0	

Table 3.2: Parameters of Model II. * The values are extracted from Table 2 of Irrgang et al. (2013). The best fit values of parameters are obtained by calculating the minimum χ^2 of constraints.

Parameters	Value*	Best fit	Derived
$M_b(10^{10}M_\odot)$	1.020675	0.93	0.93
$M_d(10^{10}M_\odot)$	7.1982	8.88	8.714
$M_h(10^{10}M_\odot)$	330.615	161.2	97.789
b_b(kpc)	0.236	0.238	
a_d(kpc)	3.262	3.712	
b_d(kpc)	0.289	0.241	
a_h(kpc)	45.02	35.164	
χ^2	2440.73	1.03	
Constraints	Observed	Best Fit	
V_r	see Bhattacharjee et al. (2014)	see Fig.3.8	
$\rho_\odot$	0.102±0.01	0.15	
$\sum_{1.1}$	74±6	68.28	

Table 3.3: Parameters of Model III. * The values are extracted from Table 3 of Irrgang et al. (2013). The best fit values of parameters are obtained by calculating the minimum χ^2 of constraints.

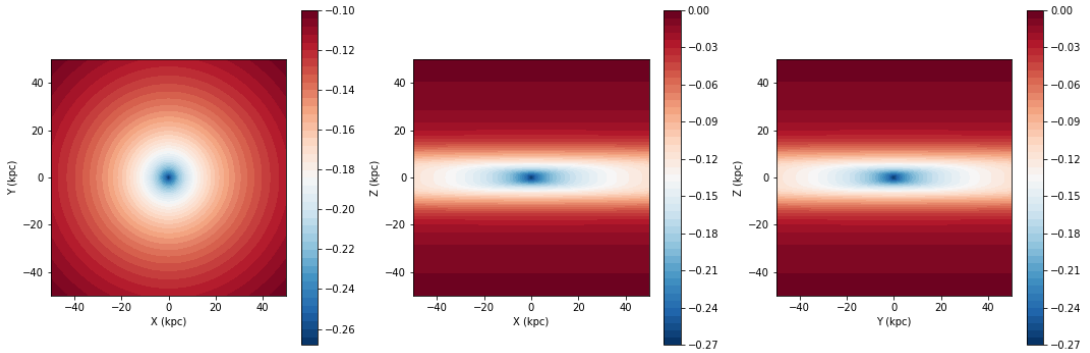

Figure 3.3: Halo potential of Model I. shown in x-y, x-z and y-z plane. The color bar is in unit of $10^{10} M_{\odot} kpc/Myr$.

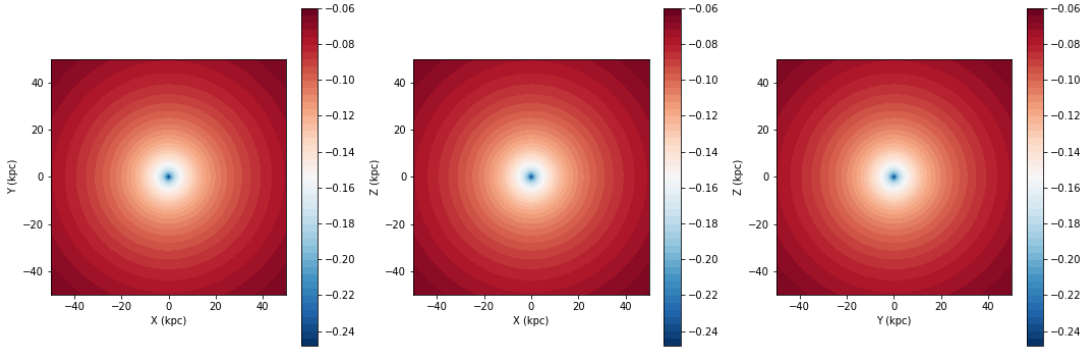

Figure 3.4: Halo potential of Model II shown in x-y, x-z and y-z plane. The color bar is in unit of $10^{10} M_{\odot} kpc/Myr$.

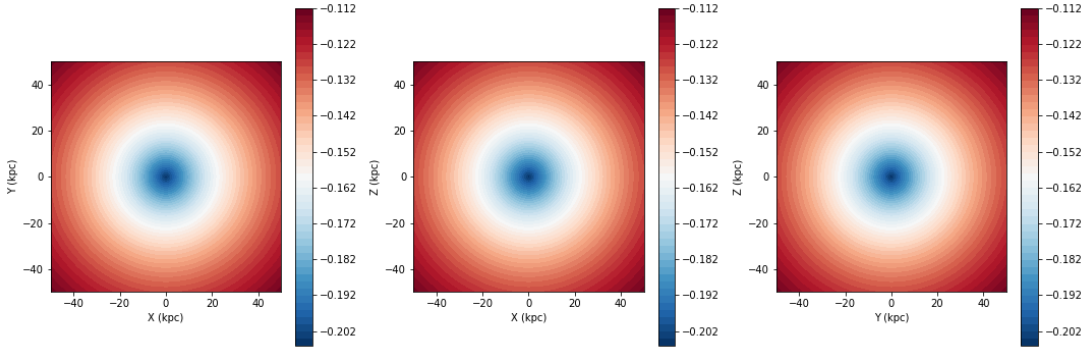

Figure 3.5: Halo potential of Model III shown in x-y, x-z and y-z plane. The color bar is in unit of $10^{10} M_{\odot} kpc/Myr$.

Bar model

To explore the orbits of GCs in the bulge, it is necessary to take into account the potential of the bar component. Ferrer's ellipsoid bar potential model is often used (e.g. Pfenniger (1984), Pichardo et al. (2004), Jílková et al. (2012), Pérez-Villegas et al. (2018)) and therefore is adopted here.

Different from the potential of bulge, disk and halo component, the bar potential depends on the time. Although we know that the bar rotates clockwise about the Galactic center, its angular velocity remains uncertain since different observation methods and models revealed different values, ranging from $40 < \Omega < 70$ km s^{-1} kpc^{-1}. If Ω = 40 km s^{-1} kpc^{-1}, it takes about 150 Myr for the bar to complete one rotation period. In addition, unlike the bulge, disk, and halo components which are axisymmetric, the bar is triaxial, dependent on the angle θ.

When calculating clusters' orbits, the bar potential is combined to the total galactic potential model, in assumption that all of the bulge mass is transferred directly to the bar component instantly.

A triaxial Ferrers bar , the density $\rho(x, y, z)$ of which is given by

$$\rho(x,y,z) = \begin{cases} \rho_c(1-m^2)^2 & \text{, if m} < 1, \\ 0 & \text{, if m} > 1, \end{cases} \tag{3.39}$$

where $\rho_c = \dfrac{105}{32\pi}\dfrac{GM_{bar}}{abc}$, M_{bar} is the total mass of the bar transferred from the mass of the bulge, and $m = \dfrac{x^2}{a^2} + \dfrac{y^2}{b^2} + \dfrac{z^2}{c^2}$. In models of astrophysics interests, the parameters a, b, c are the semi-axes of the ellipsoidal bar with $a > b > c > 0$. According to Pichardo et al. (2004), the major axis half-length $a = 3.14$ kpc, and the axial ratio $a : b : c = 10 : 3.75 : 2.56$. The present position angle of the longest axis of the bar with respect to the line of sight is 25° based on the recent results of Bovy et al. (2019).

According to Chandrasekar (1969, p.53), the potential of bar in the form of Eq.3.39 is expressed as:

$$\Phi = -\pi G abc \frac{\rho_c}{n+1} \int_\lambda^\infty \frac{du}{\Delta(u)} (1 - m^2(u))^3, \text{ where} \tag{3.40}$$

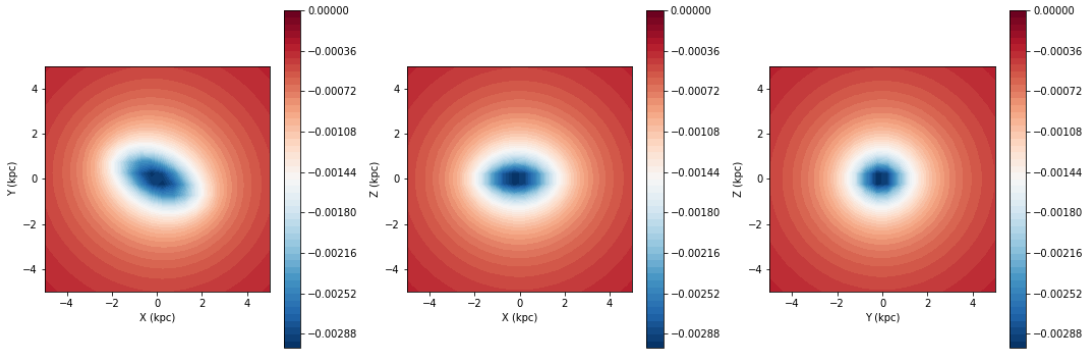

Figure 3.6: Bar potential with mass equal to $1.2\times10^{10}M_{\odot}$, shown in x-y, x-z and y-z plane respectively.

$$m^2(u) = \frac{x^2}{a^2+u} + \frac{y^2}{b^2+u} + \frac{z^2}{c^2+u}, \text{and} \tag{3.41}$$

$$\Delta^2(u) = (a^2+u)(b^2+u)(c^2+u). \tag{3.42}$$

λ is the positive solution of $m^2(\lambda) = 1$ such that outside the bar $\Phi = 0$. Inside the bar $\lambda = 0$.

3.4 Orbital Parameters

For convenience, some parameters are commonly used to describe characteristics of the Galactic orbit including its range, shape and the rotational direction. To describe the range, three parameters are usually used. For a cluster orbiting the Galaxy, the closest distance to the Galactic center is called **perigalactic distance** R_{peri}, and the farthest distance from the Galactic center is called **apogalactic distance** R_{apo}. Here, the distance to the Galactic center is defined as:

$$R = \sqrt{X^2+Y^2+Z^2} \tag{3.43}$$

, which is different from the distance in X-Y plane labelled as r:

$$r = \sqrt{X^2+Y^2} \tag{3.44}$$

The third parameter describes the maximum distance of the cluster away from the Galactic plane and is expressed as Z_{max}. Three parameters are in units of kpc. With them, we can see whether or not the cluster has entered the Galactic bulge or disk which may impact the

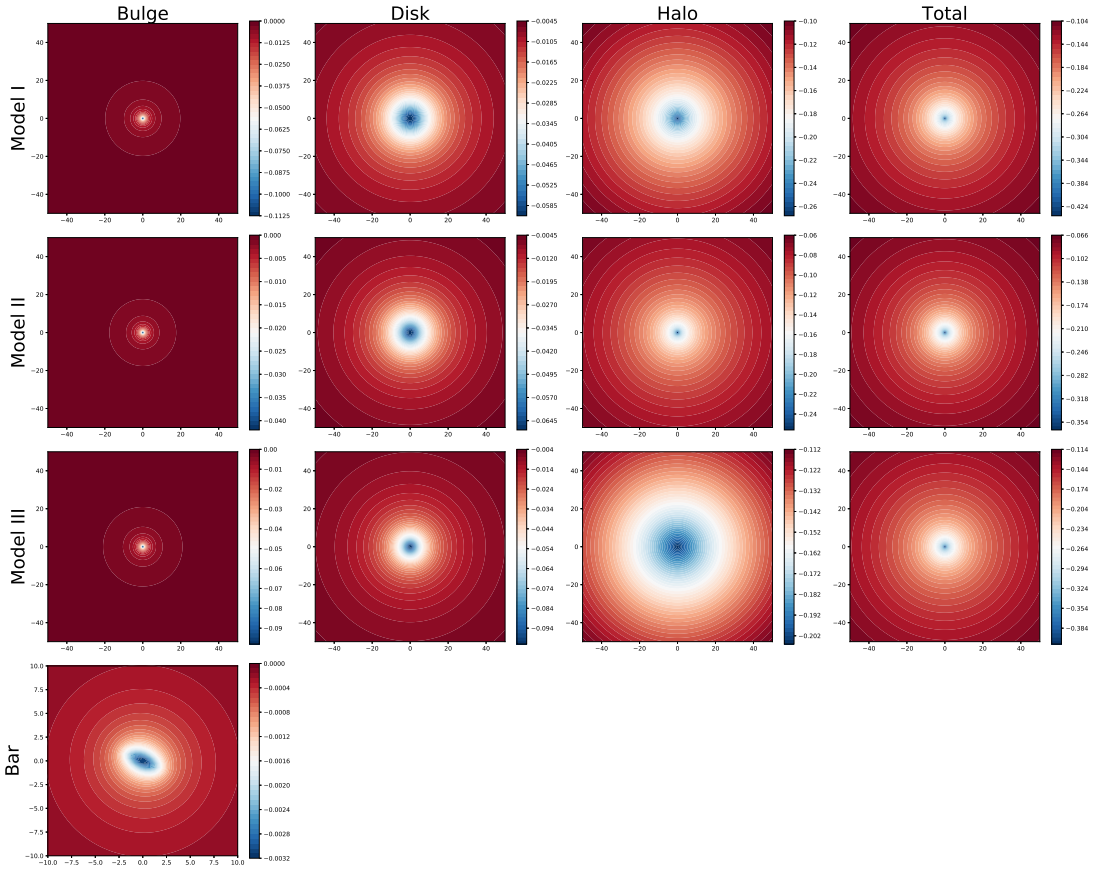

Figure 3.7: Potential components of bulge, disk,and halo in x-y plane for each model in the first three rows respectively and the bar potential in x-y plane in the last row. The color bar next to each graph shows the deepness of each potential component.

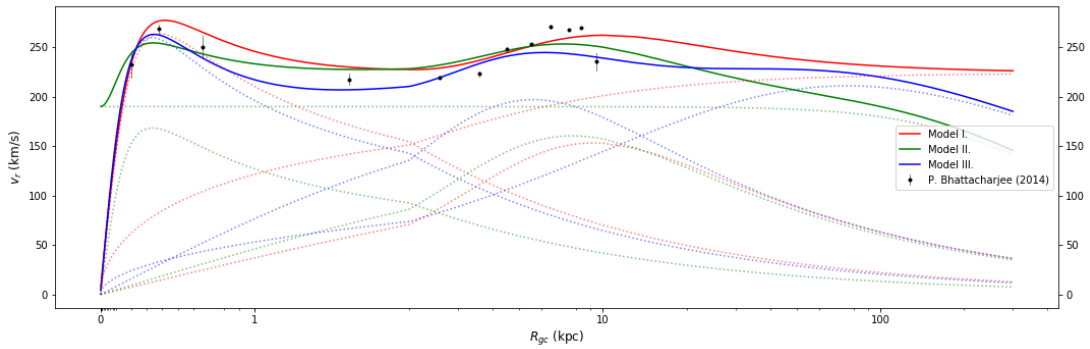

Figure 3.8: Galactic rotational curve. The color red, green, blue represent respectively potential of Model I, Model II and Model III. For each model, the contribution of galactic components: bulge contributes the most within 2kpc, the disk reached a peak at around 10 kpc, and the extended rotational curve is due to halo component. Observational data from Bhattacharjee et al. (2014) within 10 kpc is plotted in black with the error lines.

evolution of the cluster.

For the shape of an orbit, it is described by **eccentricity** which measures how much an orbit deviates from a perfect circle of the orbit, labelled as e. For a circular orbit, eccentricity is equal to zero. Elliptic orbits have $0 < e < 1$, and e = 1 is a parabolic orbit, and greater than one is a hyperbola. For clusters, most of them have elliptic orbits, and the eccentricity can be calculated from perigalactic and apogalactic distances using the following equation:

$$e = \frac{R_{apo} - R_{peri}}{R_{apo} + R_{peri}} \tag{3.45}$$

The rotational direction of cluster's orbit is an important feature since it gives hints of the formation of the cluster which is influenced by the surrounding environment. In two dimension (2D) space, it is easy to observe the direction from the cluster's tangential velocity. However, it becomes difficult to picture in 3D space and therefore angular momentum projected on the rotational axis (z-axis) is usually utilized, with positive values mean counterclockwise when viewed from the top of the z-axis. Angular momentum is defined as the cross product of the relative position vector $\vec{r}$ and the relative velocity vector v (Eq.3.47) in three dimension space:

$$\vec{L} = m\vec{R} \times v = m \begin{vmatrix} \hat{x} & \hat{y} & \hat{z} \\ X & Y & Z \\ U & V & W \end{vmatrix}, \tag{3.46}$$

$$\text{thus, } L_z = m(X \times V - Y \times U) \tag{3.47}$$

In addition, angular momentum is also significant parameters when discussing orbits. If the cluster is orbiting in a galaxy with an **axisymmetric potential** about an axis, the angular momentum projected on that axis will be conserved. To be more specific, the galactic potential applied here (Model I to III introduced in Sec. 3.3) are composed of three axisymmetric potentials including bulge, disk and halo. An axisymmetric potential doesn't have dependence on the angle θ. Therefore, when the cluster orbits in the galaxy, it won't experience the force in the direction of θ, as expressed in Eq.3.48. Consequently, there won't be any torque in the direction of z since τ_z is equal to radial distance multiply the force in θ. In addition, τ_z is equal to the time rate of change of angular momentum in the direction of z. Hence, if there is no torque in z, the angular momentum in the same direction remains

constant, as formulated in Eq.3.49.

$$\frac{\partial \Phi}{\partial \phi} = 0 = F_\theta \tag{3.48}$$

$$\tau_z = rF_\theta = \frac{dL_z}{dt} = 0, \text{ where} \tag{3.49}$$

On the other hand, the time-dependent and triaxial bar potential depends on the angle θ. Therefore when considering the bar potential, the orbital integration results won't feature conservation of L_z.

Last but not the least, when a cluster orbits in an assumed isolated galaxy, the total energy of the cluster is conserved, which is the sum of kinetic energy and total potential:

$$E = \frac{1}{2}mv^2 + \Phi \tag{3.50}$$

In order to easily identify conservation laws of energy and angular momentum in z-axis, here we define ΔE and ΔL_z:

$$\Delta E(t) = \frac{E(t) - E(t_0)}{E(t_0)}, \tag{3.51}$$

$$\Delta L_z(t) = \frac{L_z(t) - L_z(t_0)}{L_z(t_0)} \tag{3.52}$$

Here E(t) and $L_z(t)$ are energy and angular momentum at specific time t, and t_0 represents the time in the beginning. If $\Delta E(t)$ and $\Delta L_z(t)$ is equal to 0, then energy and L_z are conserved; if they are negative or positive, the values show how much they change with respect to initial values.

"Science is a way of thinking much more than it is a body of knowledge."

Carl Sagan

4

The orbit and origin of FSR1758

4.1 Tests of orbital integrators

The first and foremost step on doing orbital calculation is to confirm whether the orbital integrator applied is precise enough as integrating the orbit for a period of time. Here we take advantage of conservation laws of energy and angular momentum along z-axis to examine the precision. In the following, I compare orbits of FSR 1758 calculated from Euler, Leapfrog and GR15 to see the influence on precision of integration.

The initial conditions of the GC FSR 1758 are provided by Villanova et al. (2019) where high dispersion spectra are utilized to derive more accurate radial velocity:(α, δ, d, μ_α, μ_δ, v_r) = (262.81°, -39.82°, 11.5$\pm$ 1.0 kpc, -2.79$\pm$ 0.0097mas/yr, 2.6$\pm$ 0.009 mas/yr, 226.8$\pm$ 1.6 km/s). In the present stage the purpose is to observe influences of different integrator, thus it's not necessary to consider errors. The input initial conditions are derived using coordinate transformation introduced in Sect.3.1, which are (X, Y, Z, U, V, W) = (3.08 kpc, -2.14 kpc, -0.65 kpc, 251.71 km/s, 250.77 km/s, 198.86 km/s).

The first applied algorithm is the Euler integrator by integrating orbits backward 1.25 Gyr with 5000, 10^4 and 10^5 time steps separately. The corresponding results are shown in Fig.4.1, Fig.4.2 and Fig.4.5. To compare with the precision of different order of integration methodology, the leapfrog integrator with time steps 5000 and 10^4 (Fig.4.3, and Fig.4.4)and GR15 with time steps 1000 (Fig.4.6) are employed. Table.4.1 summarizes orbital parameters for three integrators with different time steps.

Integrator	Time steps	R_{peri} (kpc)	R_{apo} (kpc)	Z_{max} (kpc)	e	ΔE	ΔL_z	t
Euler	5×10^3	3.78	15.88	6.66	0.62	$\sim$ 0.08	$\sim$ -0.3	679 ms
Euler	10^4	3.78	13.91	5.95	0.57	$\sim$0.05	$\sim$-0.15	1.24 s
Euler	10^5	3.73	12.19	5.28	0.53	$\sim$0.006	$\sim$-0.015	12s
Leapfrog	5×10^3	3.78	13.93	5.96	0.57	$\sim$0.05	$\sim$-0.15	1.12s
Leapfrog	10^4	3.78	12.99	5.6	0.55	$\sim$0.03	$\sim$-0.08	2.1s
GR15	1×10^3	3.73	14.1	6.27	0.58	0	0	16.9 s

Table 4.1: Comparisons of orbital parameters for different integrators, including Euler, Leapfrog and GR15, and different time steps. From ΔE and ΔL_z the precision of the integrator can be quantified. T is the computational time needed to complete the calculation of orbits.

First, the comparison between three Euler orbits reveals that ΔE and ΔL_z decrease in the same extent as the number of time steps increases. This shows that as the number of time steps increases, the precision of orbital calculation becomes better. Also the larger the number of time steps is, the longer the computational time takes. Secondly, when comparing Euler with Leapfrog in the same number of time steps, Leapfrog obviously has twice better precision than Euler, but about twice calculation time is needed. Last, the result obtained from GR15 has ΔE and ΔL_z equal to 0, suggesting that GR15 is precise enough to derive orbit of the cluster with 1000 time steps. If the number is increased, the precision won't grow; instead, it leads to longer computational time.

4.2 Orbits of FSR 1758

With an integrator confirmed to be precise, the orbit of FSR 1758 can now be studied. The initial conditions applied here are the same as in the last section but errors are considered here and they are derived by using two methods:

1. Eq.3.9, which only produces errors in space velocities, and
2. Monte Carlo Simulation: by taking 10000 samples of the error distributions of initial conditions in equatorial coordinates and finding the standard deviation of the given results.

The results are shown in the inputs in upper and lower panel of Table 4.2 respectively. Then we performed orbital calculations by considering 100 samples taken randomly from normal distributions of these inputs, and three different potential models. Fig.4.7 and Fig.4.8 show the orbits obtained from input conditions of two different methods respectively, and

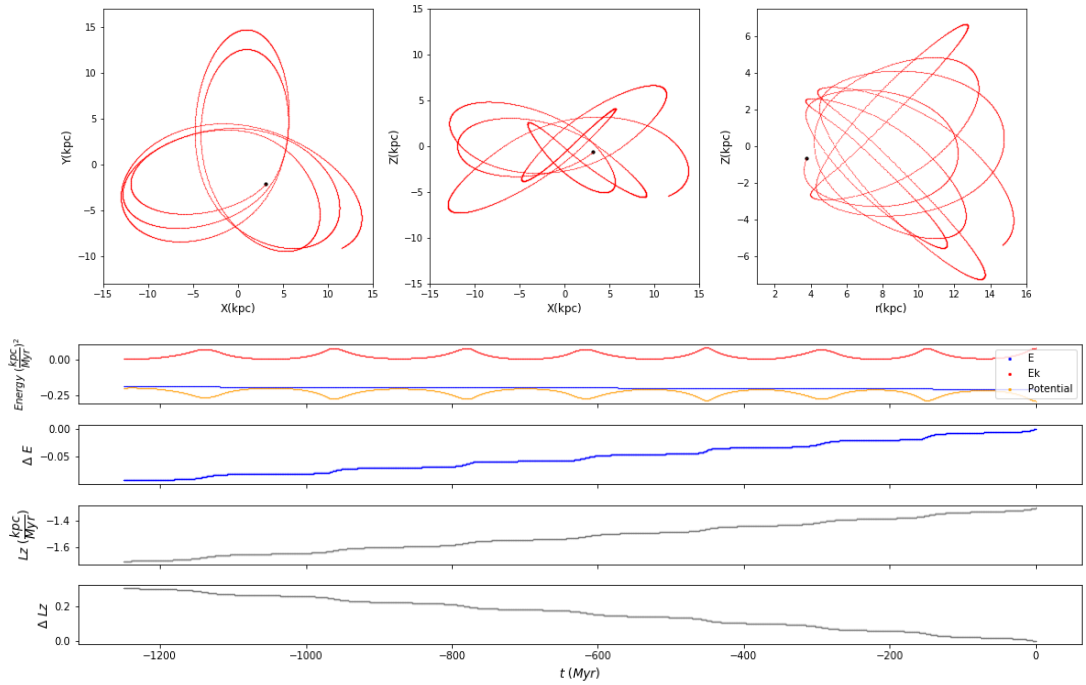

Figure 4.1: The test of Euler method with 5000 time steps: the orbits of FSR 1758 in x-y, x-z, r-z planes and its energy and L_z as a function of time, derived by integrating EoMs backward 1.25 Gyr.

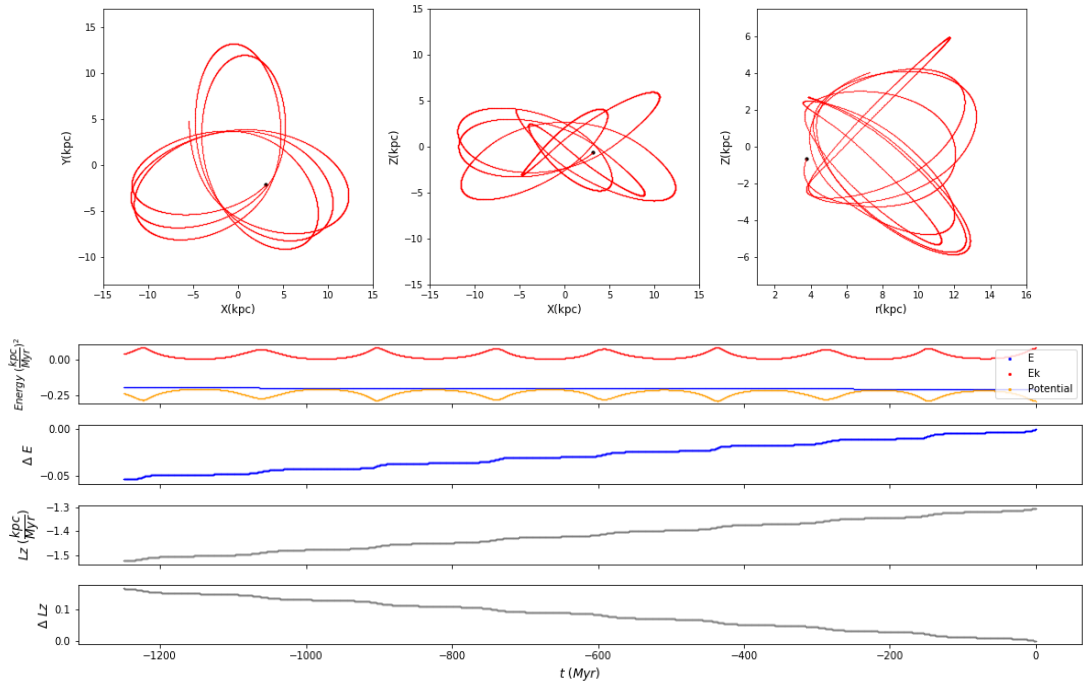

Figure 4.2: The test of Euler method with 10^4 time steps: the orbits of FSR 1758 in x-y, x-z, r-z planes and its energy and L_z as a function of time, derived by integrating EoMs backward 1.25 Gyr.

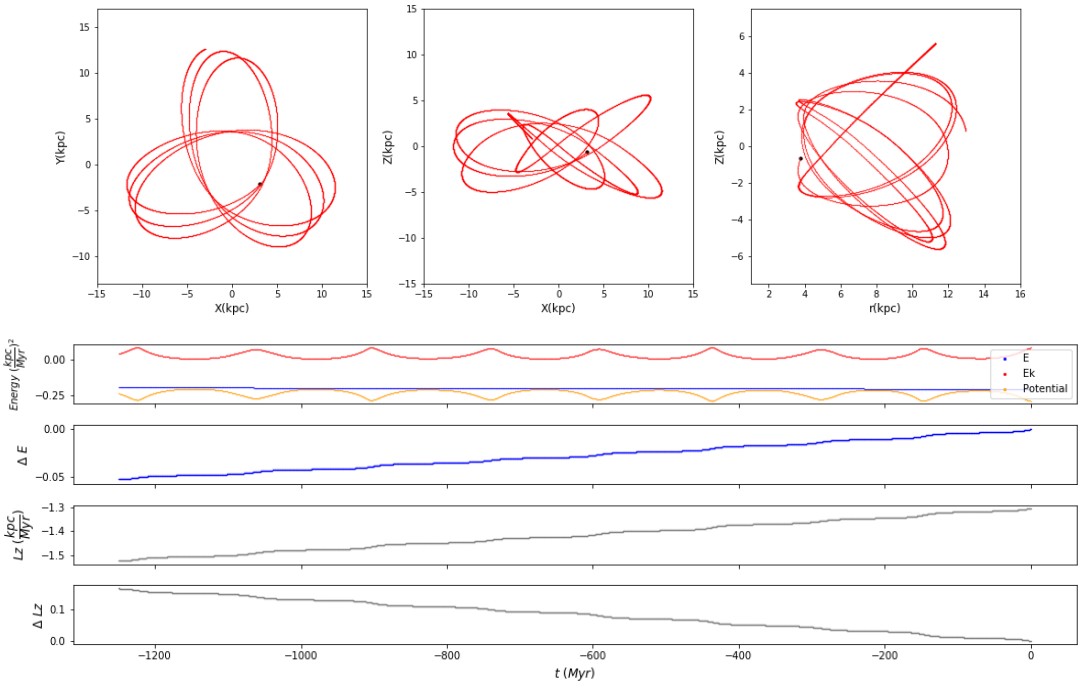

Figure 4.3: The test of Leapfrog method with 5000 time steps: the orbits of FSR 1758 in x-y, x-z, r-z planes and its energy and L_z as a function of time, derived by integrating EoMs backward 1.25 Gyr.

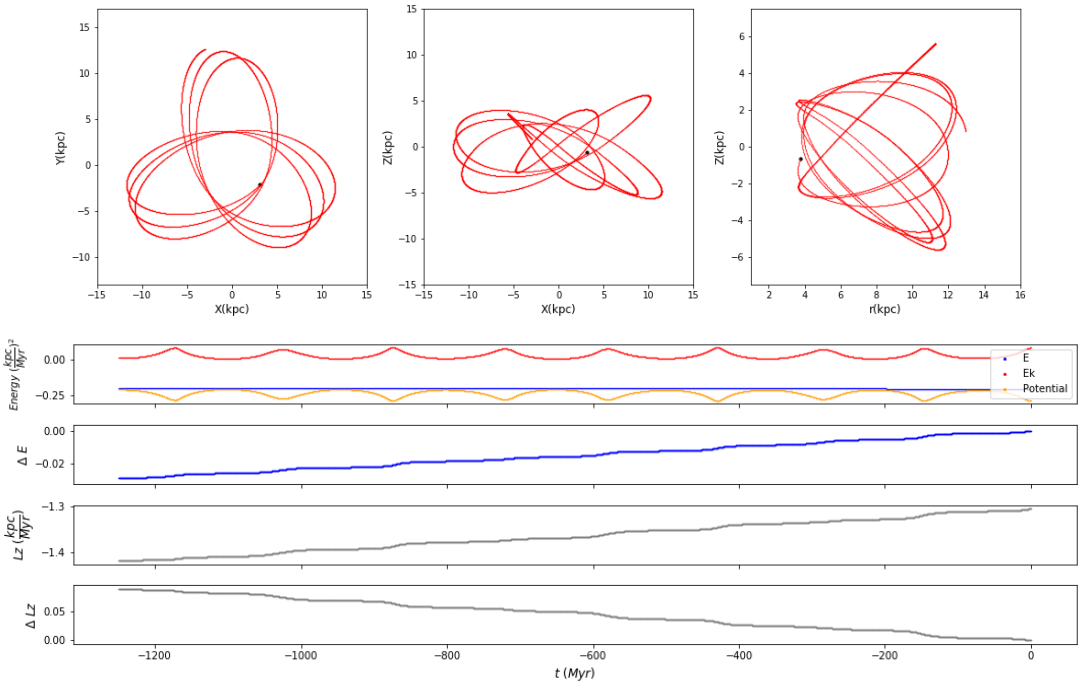

Figure 4.4: The test of Leapfrog method with 10^4 time steps: the orbits of FSR 1758 in x-y, x-z, r-z planes and its energy and L_z as a function of time, derived by integrating EoMs backward 1.25 Gyr.

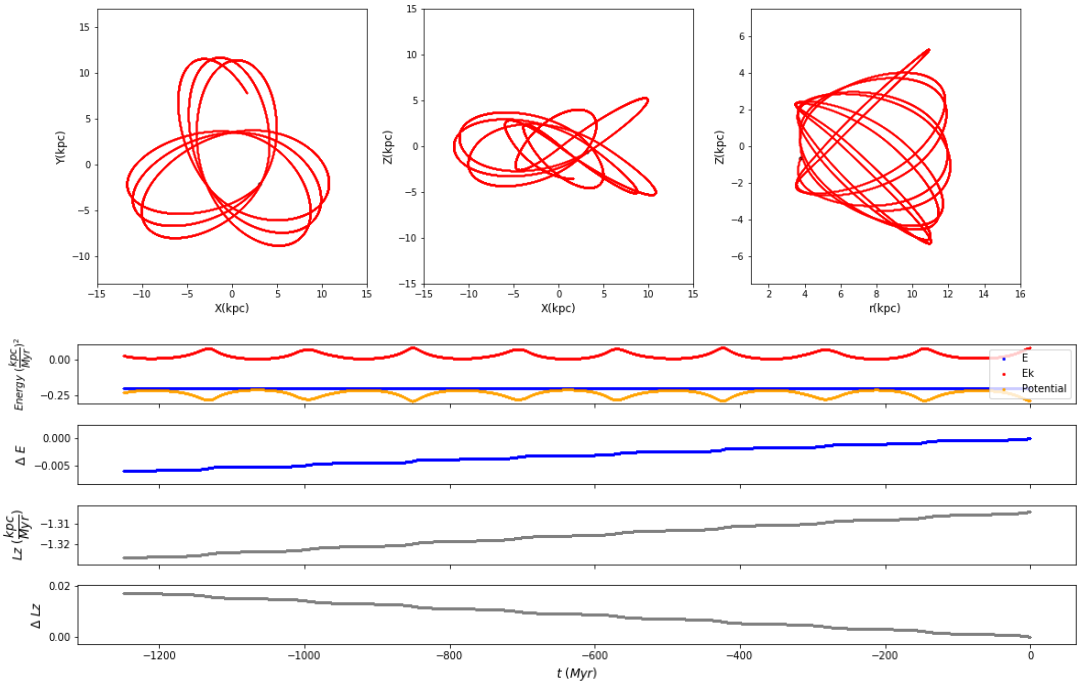

Figure 4.5: The test of Euler method with 10^5 time steps: the orbits of FSR 1758 in x-y, x-z, r-z planes and its energy and L_z as a function of time, derived by integrating EoMs backward 1.25 Gyr.

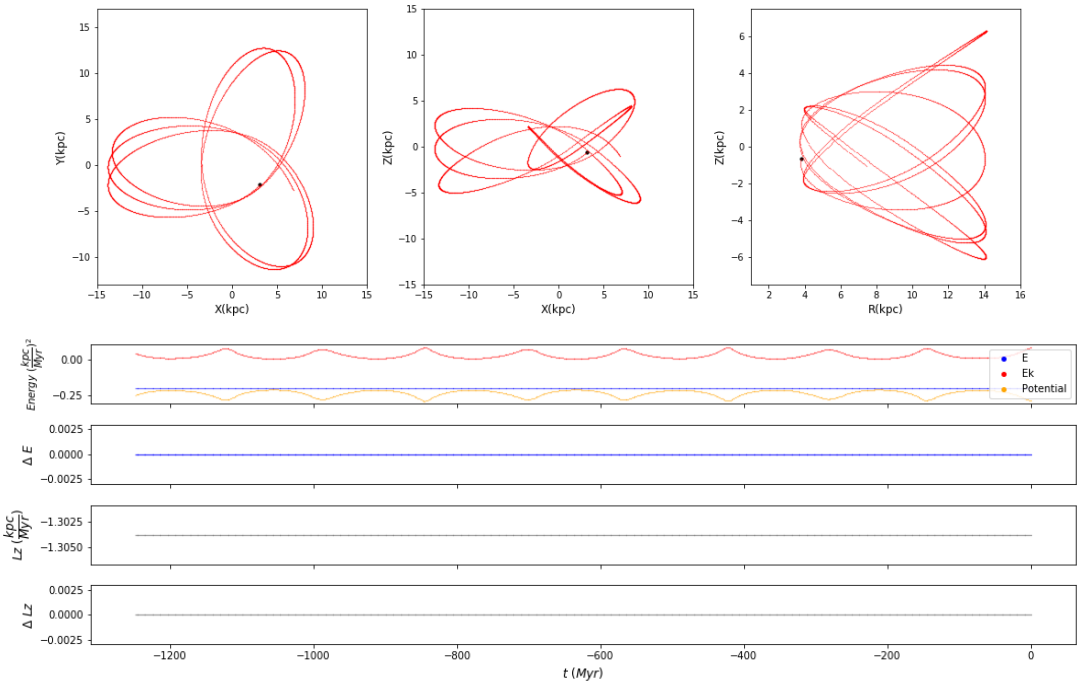

Figure 4.6: The test of GR15 with 1000 time steps: the orbits of FSR 1758 in x-y, x-z, r-z planes and its energy and L_z as a function of time, derived by integrating EoMs backward 1.25 Gyr.

Inputs	X (kpc)	Y (kpc)	Z (kpc)	U (km/s)	V (km/s)	W (km/s)
1.	3.08	-2.14	-0.65	251.71±2.24	250.77±2.9	198.86±17.8
Outputs	R_{peri}(kpc)	R_{apo}(kpc)	Z_{max}(kpc)	e	E (kpc/Myr)^2	L_z(kpc^2/Myr)
Model I	3.77±0.02	15.25±1.3	6.47±1.02	0.6±0.02	-0.16±0.004	-1.34±0.01
Model II	3.75±0.02	14.03±1.14	5.83±0.74	0.57±0.02	-0.14±0.004	-1.34±0.01
Model III	3.77±0.02	16.81±1.3	6.77±0.94	0.63±0.02	-0.19±0.004	-1.34±0.01
Inputs	X (kpc)	Y (kpc)	Z (kpc)	U (km/s)	V (km/s)	W (km/s)
2.	2.87±0.97	-2.14±0.18	-0.66±0.06	252.67±2.24	245.55±2.88	198.63±17.68
Outputs	R_{peri}(kpc)	R_{apo}(kpc)	Z_{max}(kpc)	e	E (kpc/Myr)^2	L_z(kpc^2/Myr)
Model I	3.76±0.02	15.21±1.3	6.47±1.06	0.6±0.03	-0.16±0.004	-1.34±0.009
Model II	3.58±0.86	13.84±4.9	5.95±2.56	0.58±0.04	-0.14±0.02	-1.27±0.3
Model III	3.74±0.84	17.19±5.8	7.26±3.27	0.63±0.03	-0.19±0.02	-1.32±0.3

Table 4.2: First two rows of upper and lower half table shows inputs of initial conditions by using Eq.3.1 and Monte Carlo simulations, which are labelled as 1 and 2 respectively. The last four rows in upper and lower panels show the corresponding calculated orbital parameters in three different potential models.

each of them contains orbits calculated from three potential models. Orbital parameters for three models derived from the two methods are listed in the outputs of Table 4.2.

The orbits obtained from the Monte Carlo Simulation have larger distributions in orbital parameters than the one calculated from matrices, which is reasonable because the latter one doesn't possess errors in X, Y, Z. Yet in general the results are similar, with mean R_{peri} falls outside bulge, R_{apo} far away from the center and Z_{max} goes beyond the height of Galactic thick disk. In addition, eccentricity is high about 0.6 and the cluster shows retrograde motions.

In fact, the orbit of FSR 1758 was recently studied by Simpson (2019). With averaged V_r from three stars together with proper motions from Gaia, Simpson modeled the previous 1.25 Gyr of the orbit of FSR 1578 using GALA (version 0.3; Price-Whelan 2017; Price-Whelan et al. 2018), a Python package for galactic dynamics, with the default potential "MilkyWayPotential". The potential is composed of a spherical nucleus and bulge, a Miyamoto-Nagai disk (Miyamoto and Nagai, 1975) and a spherical NFW dark matter halo (Navarro et al., 1997), similar to the Model III. The input initial conditions are (α, δ, d$_\odot$, μ_α, μ_δ, v_r) = (262.806°, -39.822°, 11.5± 1.0 kpc, -2.85± 0.1 mas/yr, 2.55± 0.1 mas/yr, 227± 1 km/s). FSR 1758 is then found to have a retrograde orbit, with R_{peri} = 3.8±0.9 kpc R_{apo} = 16^{+8}_{-5} kpc, and e=$0.62^{+0.05}_{-0.04}$, within the range of our orbits.

Next, we calculated the orbit in consideration of bar potential which may have a large influence on the orbits of clusters near the Galactic center. Since orbits distribution calcu-

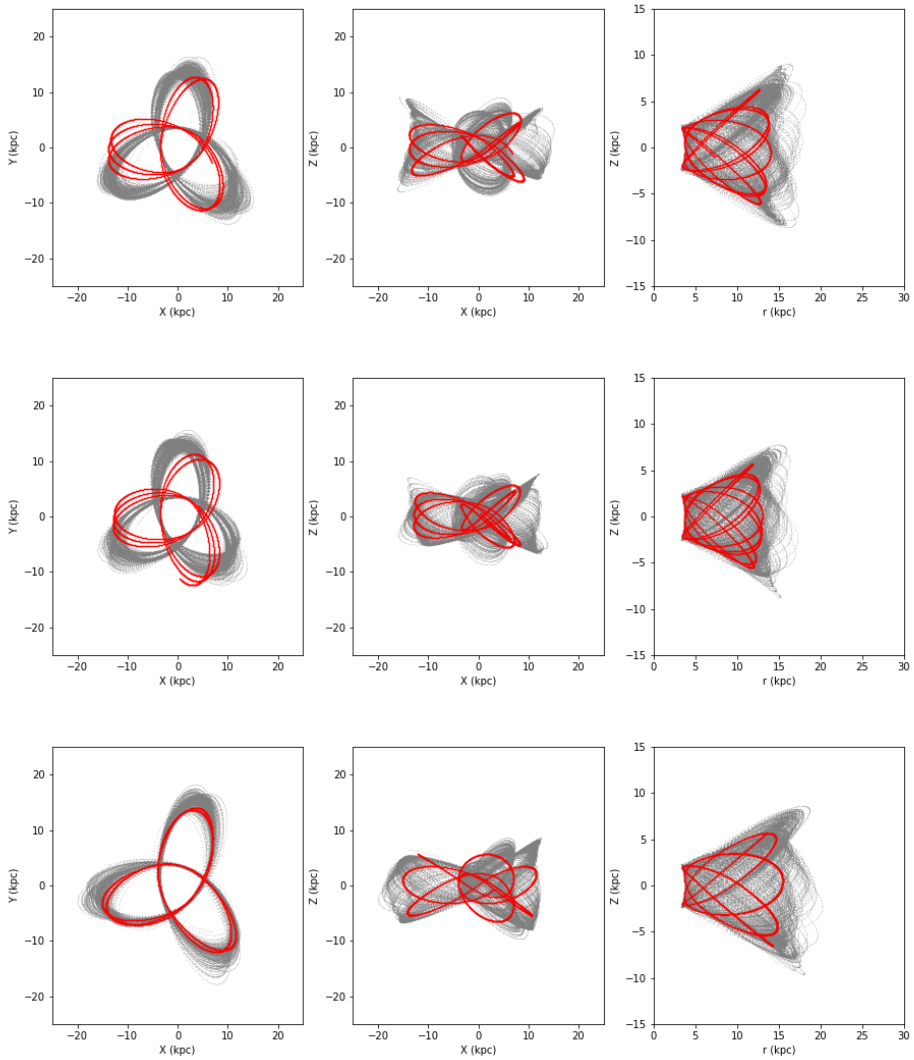

Figure 4.7: Orbits of FSR 1758 with error distributions obtained from Eq.3.1. From top to bottom are orbits calculated from Model I to Model III. The red lines are the orbit from the nominal values of the phase space coordinates. The grey lines show 100 orbits randomly sampling the error distributions of the input conditions.

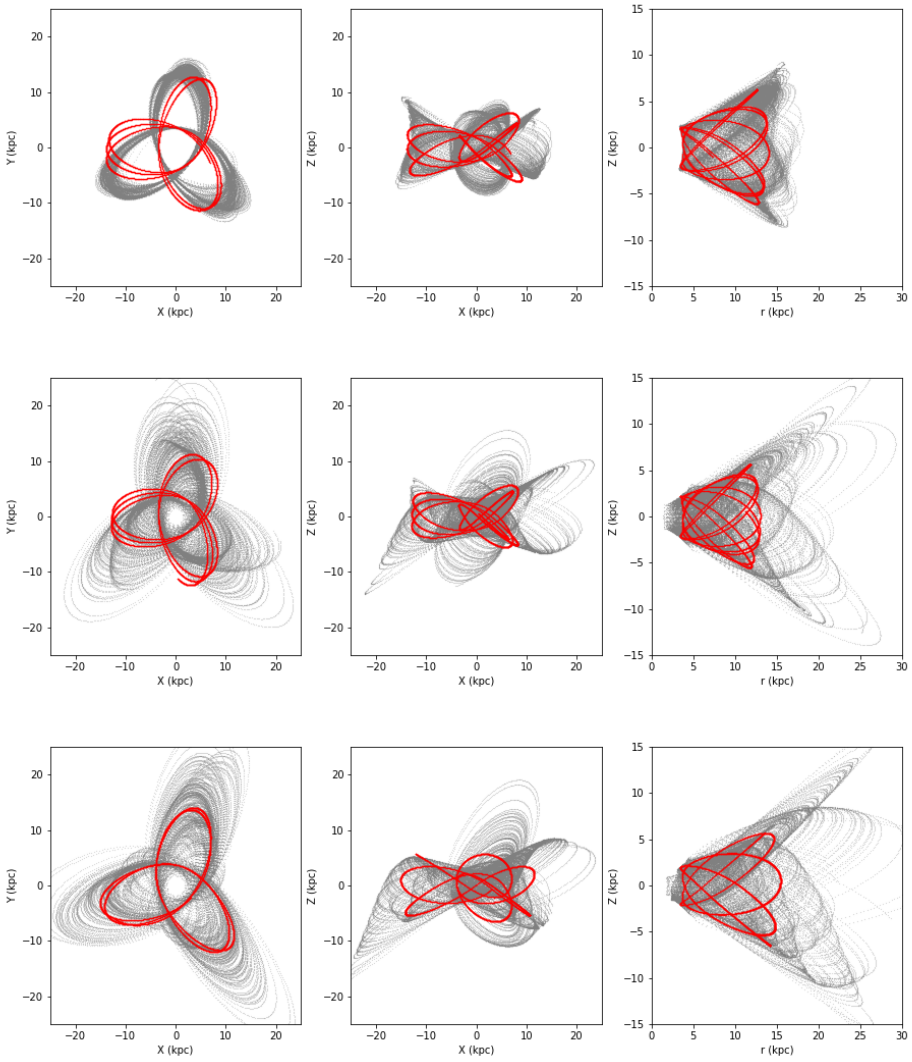

Figure 4.8: Orbits of FSR 1758 with error distributions obtained from Monte Carlo Simulations. From top to bottom are orbits calculated from Model I to Model III. The red lines are orbits from the normal values of the phase space coordinates. The grey lines show 100 orbits randomly sampling the error distributions of the input conditions.

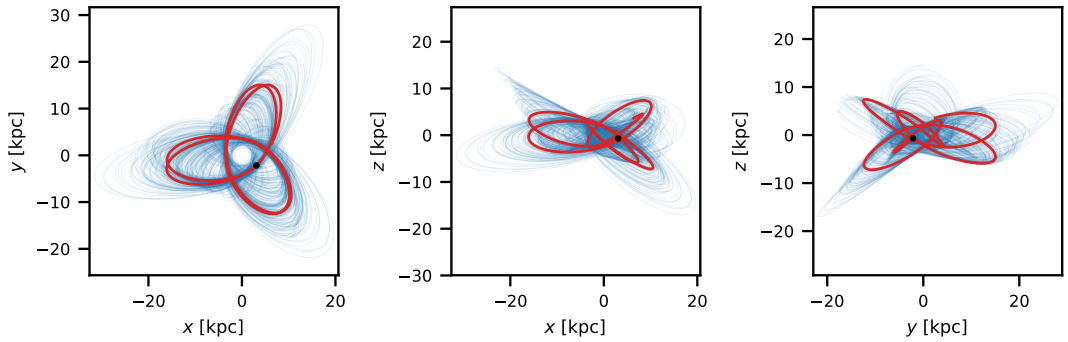

Figure 4.9: The orbits from Simpson (2019): The previous 1.25 Gyr of the orbit of FSR1758 projected into Cartesian space centred on the Galactic center. The red line is the orbit from the nominal values of the phase space coordinates, and the blue lines show 100 orbits randomly sampling the error distributions of the input parameters. The black dot shows the present position of FSR1758.

lated from Model I are more concentrated than the other two, Model II and Model III were not considered here. Besides, when comparing two methods, Model I provides the closest results. Furthermore, take notice that when adding the bar component into any model, the mass of bar is assumed to transfer from the mass of bulge all at once for simplicity, and the pattern speeds of the bar applied here are $\Omega = 41, 50, 60$ kpc^{-1} km/s. Then we integrated EoMs backward for 1.25 Gyr with 1000 time steps using GR15. Here we chose Monte Carlo simulations to consider errors.

The resulting orbital parameters are listed in Table 4.3. As we can see, different speed patterns result in similar orbital parameters. Compared with potential models without bar component, values of R_{peri}, R_{apo} and Z_{max} are similar, indicating that the time dependent bar potential doesn't influence the orbits of FSR 1758 a lot. Orbits with Ω_{bar} = 41 kpc^{-1} km/s are shown in Fig.4.10, in both Galactic frame and bar-axis frame from which we can see that **FSR 1758 didn't enter the bulge**. In addition, after including the bar, its orbits becomes more dispersed in x-y plane, which may be influenced by the rotation of the bar potential in the outer region.

4.3 The Origin of FSR1758

Whether orbits from Simpson (2019) or from the three models in this thesis, they reveal that FSR 1758 is an intruder from the Galactic halo, with R_{apo} far away from the Galactic center and Z_{max} going beyond the height of Galactic thick disk.

The origin of FSR 1758 has been studied throughout the year. It was first questioned by

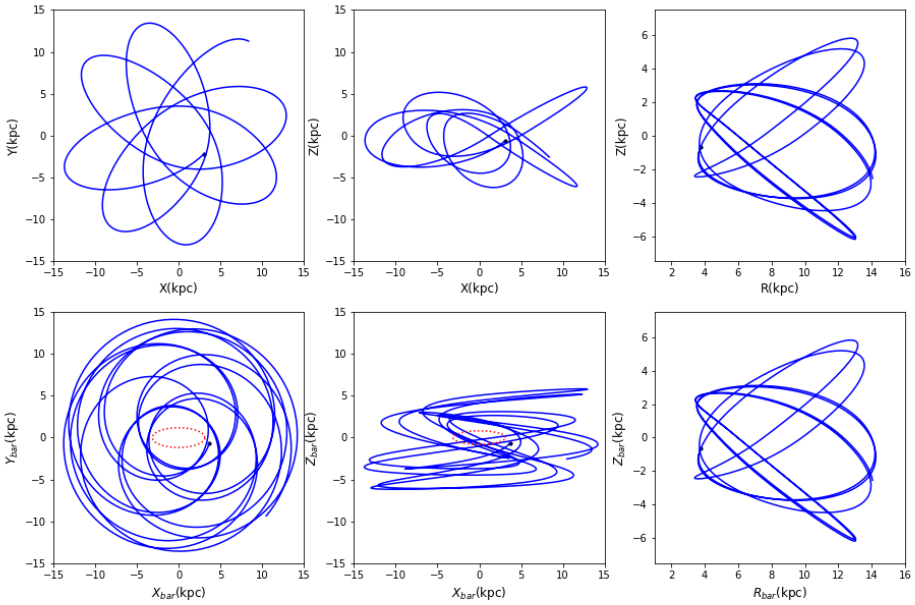

Figure 4.10: The upper panel shows Orbits of FSR 1758 in Galactic space while the lower panel shows orbits in bar-referenced space. These orbits were calculated from the potential models consisting of a disk, a halo, both of which have parameters from Model I, and a rotating bar. The bulge mass is transferred immediately to the bar when considering the bar potential, so the mass of the bar is the same as the mass of bulge in Model I. The red dash ellipse in the lower panel shows the shape of the bar. The black dot is the present location of FSR 1758.

Outputs	R_{peri}(kpc)	R_{apo}(kpc)	Z_{max}(kpc)	e	E (kpc/Myr)^2	L_z(kpc^2/Myr)
Ω=41 kpc^{-1} km/s	3.59±0.78	14.91±3.42	6.2±2.06	0.6±0.02	-0.14±0.01	-1.27±0.28
Ω=50 kpc^{-1} km/s	3.63±0.83	15.14±3.61	6.36±2.15	0.61±0.01	-0.14±0.01	-1.24±0.29
Ω=60 kpc^{-1} km/s	3.5±0.8	14.5±3.37	6±1.99	0.61±0.02	-0.14±0.01	-1.29±0.3

Table 4.3: Orbital parameters derived with three pattern speeds of bar potential. Different pattern speeds lead to similar orbital parameters, suggesting that the influence of bar potential is weak, in agreement with the fact that FSR 1758 didn't enter the bar region.

Barba et al. (2019) that whether it is a typical metal-poor GC residing in the Milky way or the central part of a dwarf galaxy. The latter assumption was supported by the common proper motions in the surrounding halo stars which could be the tidal debris of the dwarf galaxy. Soon after, Simpson (2019) argued that the halo stars are in fact not associated with the cluster because of the distinct distributions in proper motion, colour and parallax between the cluster members and the halo stars, and therefore he concluded that FSR 1758 is a GC. However, he also added that since there were no sufficient data for radial velocity and metallicity, the possibility that it is a dwarf galaxy remnant couldn't be excluded.

It is worth noting that when speaking of stars or clusters with retrograde motions or high eccentricity, they are usually linked to accretion origins. Hence, in order to investigate this relationship, we constructed plots composed of L_z in semi-logarithm scale as y-axis and eccentricity as x-axis derived by taking advantage of orbital parameters from Wu et al. (2009) for 488 OCs and Baumgardt et al. (2019) for GCs (with two exceptions Ter 10 and Djor 1 from Ortolani et al. 2019). GCs are grouped into:

1. possible accreted GCs which include events from:
   (a) Gaia Sausage (Myeong et al. 2018 and Myeong et al. 2019),
   (b) Sagittarius GCs (Forbes and Bridges, 2010),
   (c) Sequoia (Myeong et al., 2019),
   (d) Kraken (Kruijssen et al., 2019),
   (e) Canis Major (Forbes and Bridges, 2010), and
   (f) Gaia Enceladus (Helmi et al., 2018).

2. in-situ GCs:
   (a) bulge GCs listed in the Table 1. of Bica et al. 2016,
   (b) probable intruders listed in the Table 2. of Bica et al. 2016, and
   (c) lastly, GCs not belong to any of them are grouped into halo GCs.

The plots are shown in Fig.4.11 and GCs applied to each group are listed in Table 4.5.

It's interesting to find that the plots show some differentiation of these GC groups. First, the top panel compares OCs with in-situ GCs. Because most OCs were born in the disk and

In-situ	Prograde		Retrograde	
	$< L_z >$	σ_{L_z}	$<L_z>$	σ_{L_z}
OCs	1721.84	311.32	–	–
Halo	1673.87	2169.60	-1675.05	2447.72
Bulge	205.52	172.15	-54.12	13.56
Intruders	538.29	441.77	-165.84	90.65

Table 4.4: The mean angular momentum along z-axis and standard deviation of four groups of GCs formed in-situ. Units of L_z and σ_{L_z} are in kpc km/s.

rotate the Galaxy in a nearly circular clockwise orbits, they concentrate at high L_z ($\geq 10^3$) and low eccentricity. However, unlike OCs, GCs in general are more dispersed in L_z and e and occupy both prograde and retrograde orbits. Bulge GCs have $L_z < 10^3$. On the other hand, halo GCs have higher L_z in average yet with wider distribution. Lower L_z of bulge GCs than the halo GCs agrees with the bulge formation scenario of dissipative collapse, during which low angular momentum gas collapsed towards the central parts of the Galaxy. Possible intruder GCs seem to connect previous two groups. Values of the mean L_z and standard deviation for the three groups are provided in Table 4.4.

In the middle and bottom of Fig.4.11 show different grouping of GCs from different accretion events proposed by several authors. Most of the accreted GCs have eccentricity higher than 0.5. Particularly, Gaia Sausage, Sequoia and Sagittarius GCs in the middle panel show clearer grouping feature in eccentricity, e = 0.4-0.6 for the first two and 0.8-1.0 for the last one. In addition, apart from Gaia Sausage group which has a ratio of prograde/retrograde orbits 13/8, Sagittarius and Sequoia groups hold 100% prograde and 100% retrograde motion respectively. However, in Kraken, Canis Major and Gaia Enceladus groups, GCs in each of them don't seem to relate to each other that much, with prograde and retrograde orbits mix together in a wide range of eccentricity. Some GCs even overlap between the groups. Especially, most Gaia Enceladus GCs exhibit similar distribution as Gaia Sausage GCs, in agreement with Piatti (2019) who probed accretion events using the inclination and the eccentricity of GCs.

As a consequence, it should be noted that GCs with retrograde or high eccentricity orbits are not special cases at all. For a system with high random motions, the mixing of prograde and retrograde orbits and the presence of high eccentricity orbits is reasonable. What's more important issues here are that, **first these accreted GCs should possess similar kinematics behaviors since they were from the same original host which gravitationally bound them together, and therefore when the merging happened their collective behaviors**

would be preserved due to the sparse density in the outer halo region; and second, **whether these collective behaviors are distinct enough from the Milky Way to be indications of relics of accretion events.**

Back to our main target, from the first and second plots of Fig.4.11, FSR 1758 locates in the range of Sequoia group as well as in-situ halo GCs. Myeong et al. (2019) has suggested FSR 1758 to be one of members of Sequoia based on the distribution in action spaces. Here, though there are only five GCs in the Sequoia event, the probability that the clustering is a signature of accretion events couldn't be ruled out. Hence FSR 1758 could be one of GCs in Sequoia dwarf galaxy accreted to the Milky Way. Similarly, because there are only five GCs, this evidence is not strong enough to support the clustering behavior. An in-situ origin for the cluster is also possible.

In kinematics, the origin of FSR 1758 could be a halo intruder or accreted from Sequoia event. However, just recently Villanova et al. (2019) further analyzed chemical components of FSR 1758 in detail by using high dispersion spectra for 9 stars and discovered the Na-O anti-correlation of metal-poor GCs which is found for all metal-poor GCs . According to them, the two components fit the mean Na and O abundance of other halo GCs very well when the second generation stars in them are excluded. When considering all stars, depletion in O and enhancement in Na came out. Apart from this, its α elements display the same trend with Galactic GCs as well as halo and thick disk stars and the trend is not commonly seen in extra-galactic objects. As a consequence, FSR 1758 is more similar to in-situ halo GCs in aspect of chemical abundance.

Accretion Events	Candidate GCs	Sources
Gaia Sausage	NGC 1851[1], NGC 1904[1], NGC 2298[1], NGC 2808[1], NGC 5286[1], NGC 6779[1], NGC 6864[1], NGC 7089[1], NGC 362[1] , NGC 1261[1], NGC 4147[2], NGC 4833[2], NGC 5694[2], NGC 6544[2], NGC 6584[2], NGC 6712[2], NGC 6934[2], NGC 6981[2], NGC 7006[2], Pal 14[2], Pal 15[2].	[1]Myeong et al. (2018) , [2]Myeong et al. (2019)
Sequoia	FSR 1758, NGC 3201, NGC 5139, NGC 6101, NGC 5635, NGC 6388	Myeong et al. (2019)
Sagittarius	Ter 7, Arp 2, Ter 8, NGC 6715, NGC 4147, NGC 5634, Pal 12, AM 4, Whiting 1.	Forbes and Bridges (2010)
Kraken	NGC 362, NGC 1261, NGC 3201, NGC 5139, NGC 5272, NGC 5897, NGC 5904, NGC 5946, NGC 6121, NGC 6284, NGC 6544, NGC 6584, NGC 6752, NGC 6864, NGC 6934.	Kruijssen et al. (2019)
Canis Major	NGC 1851, NGC 1904, NGC 2808, NGC 4590, NGC 6341, IC 4499, NGC 6205, NGC 5286, NGC 6779, NGC 7078.	Forbes and Bridges (2010)
Gaia Enceladus	NGC 288, NGC 362, NGC 1851, NGC 1904, NGC 2298, NGC 4833, NGC 5139, NGC 6205, NGC 6341, NGC 6779, NGC 7089, NGC 7099.	Helmi et al. (2018)
In- Situ	Candidate GCs	Sources
Bulge	Ter 3, ESO 452-SC11, NGC 6256, NGC 6266, NGC 6304, NGC 6316, NGC 6325, NGC 6342, NGC 6355, Ter 2, Ter 4, HP 1, Lil 1, Ter 1, Ton 2, NGC 6401, Pal 6, Ter 5, NGC 6440, Ter 6, UKS 1, Ter 9, Djor 2, NGC 6522, NGC 6528, NGC 6539, NGC 6540, NGC 6553, NGC 6558, NGC 6569, BH 261, Mercer 5, NGC 6624, NGC 6626, NGC 6638, NGC 6637, NGC 6642, NGC 6652, NGC 6717, NGC 6723	Table 1 of Bica et al. (2016).
Intruders	Lynga 7, NGC 6144, NGC 6171, NGC 6235, NGC6273,NGC 6287, NGC 6293, NGC 6352, NGC 6380, NGC 6388, NGC 6402, NGC 6441, NGC 6496, NGC 6517, NGC 6544, 2MS 2, IC 1276, Ter 12, NGC 6712.	Table 2 of Bica et al. (2016)
Halo	NGC 104, AM 1, Eridanus, Pal 2, NGC 2419, Pyxis, E 3, Pal 3, Pal 4, Crater, NGC 4372, NGC 5024, NGC 5053, NGC 5466, NGC 5824, Pal 5, NGC 5927, NGC 5986, FSR 1716, NGC 6093, NGC 6139, NGC 6229, NGC 6218, FSR 1735, NGC 6254, NGC 6333, NGC 6356, IC 1257, NGC 6366, NGC 6362, NGC 6397, NGC 6426, Djor 1*, Ter 10*, NGC 6535, NGC6541, ESO 280, Pal 8, NGC 6656, NGC 6681, NGC 6749, NGC 6760, Pal 10, NGC 6809, Pal 11, NGC 6836, Pal 13, NGC 7492.	GCs in Baumgardt et al. (2019) not listed in any of previous group. * Orbital paremeters of Djor 1 and Ter 10 are taken from Ortolani et al. (2019) since it has more reliable distance measurements than Baumgardt et al. (2019) in which Ter 10 was revealed to be a bulge cluster. However, according to Ortolani et al. (2019) it's a halo intruder.

Table 4.5: Lists of accreted and in-situ GCs categorized into different groups.

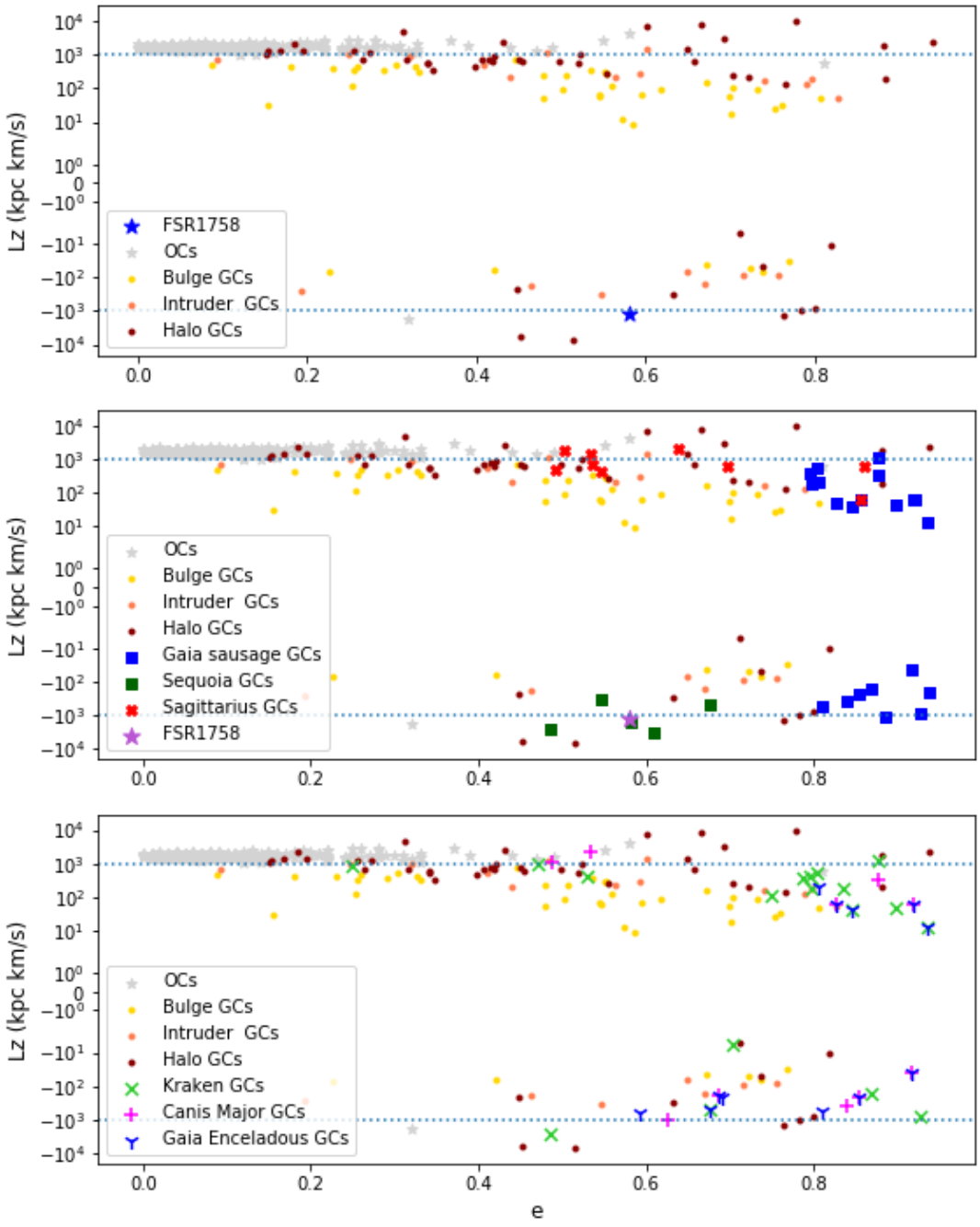

Figure 4.11: Relationships between the angular momentum along z direction L_z versus eccentricity e for the GC groups. Top panel: In-situ GCs associated with the Galactic halo, bulge or intruders into the bulge in comparison with OCs. Middle panel: GCs from three accretion events, Gaia Sausage, Sequoia and Sagittarius, compared with in-situ GCs and OCs. Bottom panel: GCs from three accretion events, Kraken, Canis Major and Gaia Enceladus, compared with in-situ GCs and OCs.

The end of one journey is the beginning of the another.

Joseph M. Marshall III

5 Conclusions

As a giant cluster hidden behind the high extinction Galactic bulge with a distance 11.5±1.0 kpc (Barba et al., 2019) from us, FSR 1758 has been paid much attention recently. It was discovered due to its prominent proper motions from the field stars, and the presence of RGB, RGBb and BHB in optical and near-IR CMDs (Cantat-Gaudin et al. 2018, Barba et al. 2019 and Simpson 2019) lead to the consensus of FSR 1758 as a metal-poor GC. Its metalliity was confirmed by Villanova et al. (2019) with a value [Fe/H]= -1.58 $\pm$ 0.03 dex by using high resolution spectra. This latest observation of FSR1758 gives (α, δ, $d_{\odot}$, μ_{α}, μ_{δ}, v_r) = (262.81°, -39.82°, 11.5 $\pm$ 1.0 kpc, -2.79 $\pm$ 0.0097 mas/yr, 2.6 $\pm$ 0.009 mas/yr , 226.8 $\pm$ 1.6 km/s. From these parameters we derived the position and velocity in Galactocentric Cartesian coordinate through Monte Carlo Simulation: (X, Y, Z, U, V, X) = (2.87 $\pm$ 0.97 kpc, -2.14 $\pm$ 0.18 kpc, -0.66 $\pm$ 0.06 kpc, 252.67 $\pm$ 2.24 km/s, 245.55 $\pm$ 2.88 km/s, 198.63 $\pm$ 17.68 km/s).

In the thesis, the orbits of FSR 1758 were derived in three different galactic potential models through integrating EoMs backward for 1.25 Gyr with an efficient and precise algorithm: Gauss-Radau spacings of 15^{th} order. The resulting orbits are in agreement with the one in Simpson (2019), having orbital parameters 3 kpc $< R_{peri} <$ 4 kpc, 14 kpc $< R_{apo} <$ 16 kpc, $Z_{max} \sim$ 6 kpc and e $\sim$ 0.6. Furthermore, a potential with bar component was then added to observe its influence on the cluster orbit. It is assumed that the mass of the bar is transferred from the mass of the bulge instantly. When being viewed in the bar-axis reference, the cluster didn't enter the inner region of the bar, matching the fact that there are no

significant changes in orbital parameters.

Because its apogalactic distance is far away from the Galactic center and the maximum height of its orbit exceeds the height of Galactic thick disk, FSR 1758 is believed to be an intruder from the Galactic halo. However, whether it is an in-situ GC that formed inside the Galactic halo or belongs to one of accreted GCs left over after the merger of satellite dwarf galaxies into the Milky Way was unclear. FSR 1758 possess both retrograde and high eccentricity properties that are thought to be signatures of accretion events.

To probe the relationship between them, we grouped 154 GCs into accreted and not accreted then plotted L_z-e space. Accreted GCs were then categorized into 6 well-known accretion events based on literature. They are Gaia Sausage, Sequoia, Sagittarius , Canis Major, Kraken and Gaia Enceladus. Not accreted GCs were separated into bulge GCs (with $R_{apo} <$ 3kpc), intruders based on metallicity and distance (Bica et al., 2016) and halo GCs that don't belong to bulge, intruders or any accreted event.

The results (Fig.4.11) show that in the cases of Sagittarius, Gaia Sausage and Sequoia, they share the feature of concentrated, high eccentricity. However, retrograde orbit is not a peculiar feature for accretion events anymore. All GCs in Sagittarius have prograde orbits while all GCs in Sequoia have retrorgrade orbits. What's more surprising is that Gaia Sausage owns both prograde and retrograde orbits of very high eccentricity, in line with the statement that it is a head-on collision event.

In the cases of Canis Major, Kraken and Gaia Enceladus, they exhibit more spread eccentricity but mostly higher than 0.5. Prograde and retrograde orbits are mixed together. Though having less grouping characteristics, they show overlapping with other events, especially Gaia Sausage mostly. This probably suggests that different accretion groups may be in fact come from the same merging event.

For FSR 1758, it falls in the region of Sequoia event. Although Sequoia GCs seem to be confined in a small region, there are only four candidates GCs in this event. As a consequence, we can't be sure if FSR 1758 is really from Sequoia or it is just a coincidence for four in-situ halo GCs. Nevertheless, with the help of detailed chemical abundance analysis done by Villanova et al. (2019), FSR 1758 was found to contain similar trend in α elements and Na-O anti-correlation for metal-poor halo GCs. Therefore, the origin of FSR 1758 is most probably a halo GC formed inside the Milky Way .

In summary, thanks to previous studies of FSR 1758 from many aspects, FSR 1758 is concluded to be a genuine halo GCs.

References

Allen, C. and Martos, M. A. (1986). A simple, realistic model of the galactic mass distribution for orbitcomputations. , 13:137–147.

Allen, C. and Santillan, A. (1991). An improved model of the galactic mass distribution for orbit computations. , 22:255.

Armandroff, T. E. (1989). The Properties of the Disk System of Globular Clusters. , 97:375.

Barba, R. H., Minniti, D., Geisler, D., Alonso-García, J., Hempel, M., Monachesi, A., Arias, J. I., and Gómez, F. A. (2019). A Sequoia in the Garden: FSR 1758—Dwarf Galaxy or Giant Globular Cluster? , 870(2):L24.

Baumgardt, H., Hilker, M., Sollima, A., and Bellini, A. (2019). Mean proper motions, space orbits, and velocity dispersion profiles of Galactic globular clusters derived from Gaia DR2 data. , 482(4):5138–5155.

Belokurov, V., Erkal, D., Evans, N. W., Koposov, S. E., and Deason, A. J. (2018). Co-formation of the disc and the stellar halo. , 478(1):611–619.

Bhattacharjee, P., Chaudhury, S., and Kundu, S. (2014). Rotation Curve of the Milky Way out to ~200 kpc. , 785(1):63.

Bica, E., Ortolani, S., and Barbuy, B. (2016). Globular Clusters in the Galactic Bulge. , 33:e028.

Bland-Hawthorn, J. and Gerhard, O. (2016). The Galaxy in Context: Structural, Kinematic, and Integrated Properties. , 54:529–596.

Bovy, J. (2011). *Dynamical Inference in the Milky Way*. PhD thesis, New York University.

Bovy, J., Leung, H. W., Hunt, J. A. S., Mackereth, J. T., Garcia-Hernandez, D. A., and Roman-Lopes, A. (2019). Life in the fast lane: a direct view of the dynamics, formation, and evolution of the Milky Way's bar. *arXiv e-prints*, page arXiv:1905.11404.

Cantat-Gaudin, T., Jordi, C., Vallenari, A., Bragaglia, A., Balaguer-Núñez, L., Soubiran, C., Bossini, D., Moitinho, A., Castro-Ginard, A., Krone-Martins, A., Casamiquela, L., Sordo, R., and Carrera, R. (2018). A Gaia DR2 view of the open cluster population in the Milky Way. , 618:A93.

Côté, P. (1999). Kinematics of the Galactic Globular Cluster System: New Radial Velocities for Clusters in the Direction of the Inner Galaxy. *The Astronomical Journal*, 118(1):406–420.

Djorgovski, S. (1993). Physical Parameters of Galactic Globular Clusters. In Djorgovski, S. G. and Meylan, G., editors, *Structure and Dynamics of Globular Clusters*, volume 50 of *Astronomical Society of the Pacific Conference Series*, page 373.

Everhart, E. (1985). An efficient integrator that uses Gauss-Radau spacings. In Carusi, A. and Valsecchi, G. B., editors, *IAU Colloq. 83: Dynamics of Comets: Their Origin and Evolution*, volume 115, page 185.

Forbes, D. A. and Bridges, T. (2010). Accreted versus in situ Milky Way globular clusters. , 404(3):1203–1214.

Frenk, C. S. and White, S. D. M. (1982). The form of the galactic globular cluster system and the distance to the galactic centre. , 198:173–192.

Froebrich, D., Scholz, A., and Raftery, C. L. (2007). A systematic survey for infrared star clusters with |b| <20° using 2MASS. , 374(2):399–408.

Gaia Collaboration, Brown, A. G. A., Vallenari, A., Prusti, T., de Bruijne, J. H. J., Babusiaux, C., Bailer-Jones, C. A. L., Biermann, M., Evans, D. W., Eyer, L., and et al. (2018). Gaia Data Release 2. Summary of the contents and survey properties. , 616:A1.

Gilmore, G. and Reid, N. (1983). New light on faint stars - III. Galactic structure towards the South Pole and the Galactic thick disc. , 202:1025–1047.

Gratton, R., Sneden, C., and Carretta, E. (2004). Abundance Variations Within Globular Clusters. , 42(1):385–440.

Gratton, R. G., Carretta, E., and Bragaglia, A. (2012). Multiple populations in globular clusters. Lessons learned from the Milky Way globular clusters. , 20:50.

Gregersen, E. (2010). *The Milky Way and Beyond: Stars, Nebulae, and Other Galaxies* .

Harris, W. E. (1976). Spatial structure of the globular cluster system and the distance to the galactic center. , 81:1095–1116.

Harris, W. E. (1996). VizieR Online Data Catalog: Globular Clusters in the Milky Way (Harris, 1996). *VizieR Online Data Catalog*, page VII/195.

Harris, W. E. (2010). A New Catalog of Globular Clusters in the Milky Way. *arXiv e-prints*, page arXiv:1012.3224.

Helmi, A., Babusiaux, C., Koppelman, H. H., Massari, D., Veljanoski, J., and Brown, A. G. A. (2018). The merger that led to the formation of the Milky Way's inner stellar halo and thick disk. , 563(7729):85–88.

Holmberg, J. and Flynn, C. (2000). The local density of matter mapped by Hipparcos. , 313(2):209–216.

Holmberg, J. and Flynn, C. (2004). The local surface density of disc matter mapped by Hipparcos. , 352(2):440–446.

Ibata, R. A., Gilmore, G., and Irwin, M. J. (1994). A dwarf satellite galaxy in Sagittarius. , 370(6486):194–196.

Irrgang, A., Wilcox, B., Tucker, E., and Schiefelbein, L. (2013). Milky Way mass models for orbit calculations. , 549:A137.

Jílková, L., Carraro, G., Jungwiert, B., and Minchev, I. (2012). The origin and orbit of the old, metal-rich, open cluster NGC 6791. Insights from kinematics. , 541:A64.

Johnson, D. R. H. and Soderblom, D. R. (1987). Calculating Galactic Space Velocities and Their Uncertainties, with an Application to the Ursa Major Group. , 93:864.

King, I. (1962). The structure of star clusters. I. an empirical density law. , 67:471.

Kinman, T. D. (1959). Globular clusters, II. The spectral types of individual stars and of the integrated light. , 119:538.

Kruijssen, J. M. D., Pfeffer, J. L., Reina-Campos, M., Crain, R. A., and Bastian, N. (2019). The formation and assembly history of the Milky Way revealed by its globular cluster population. , 486(3):3180–3202.

Minniti, D. (1996). Field Stars and Clusters of the Galactic Bulge: Implications for Galaxy Formation. *The Astrophysical Journal*, 459:175.

Minniti, D., Saito, R. K., Gonzalez, O. A., Alonso-García, J., Rejkuba, M., Barbá, R., Irwin, M., Kammers, R., Lucas, P. W., Majaess, D., and Valenti, E. (2018). A new near-IR window of low extinction in the Galactic plane. , 616:A26.

Miyamoto, M. and Nagai, R. (1975). Three-dimensional models for the distribution of mass in galaxies. , 27:533–543.

Morgan, W. W. (1959). The Differences Among Globular Clusters: The integrated spectra of globular clusters. , 64:432–436.

Myeong, G. C., Evans, N. W., Belokurov, V., Sand ers, J. L., and Koposov, S. E. (2018). The Sausage Globular Clusters. , 863(2):L28.

Myeong, G. C., Vasiliev, E., Iorio, G., Evans, N. W., and Belokurov, V. (2019). Evidence for two early accretion events that built the Milky Way stellar halo. , 488(1):1235–1247.

Navarro, J. F., Frenk, C. S., and White, S. D. M. (1997). A Universal Density Profile from Hierarchical Clustering. , 490(2):493–508.

Ortolani, S., Nardiello, D., Pérez-Villegas, A., Bica, E., and Barbuy, B. (2019). Halo intruders in the Galactic bulge revealed by HST and Gaia: the globular clusters Terzan 10 and Djorgovski 1. , 622:A94.

Pérez-Villegas, A., Rossi, L., Ortolani, S., Casotto, S., Barbuy, B., and Bica, E. (2018). Orbits of Selected Globular Clusters in the Galactic Bulge. , 35:e021.

Pfenniger, D. (1984). The 3D dynamics of barred galaxies. , 134(2):373–386.

Piatti, A. E. (2019). Formation imprints in the kinematics of the Milky Way globular cluster system. *arXiv e-prints*, page arXiv:1907.09824.

Pichardo, B., Martos, M., and Moreno, E. (2004). Models for the Gravitational Field of the Galactic Bar: An Application to Stellar Orbits in the Galactic Plane and Orbits of Some Globular Clusters. , 609(1):144–165.

Price-Whelan, A., Sipocz, B., Daniel, Major, S., and Oh, S. (2018). adrn/gala: v0.3.

Price-Whelan, A. M. (2017). Gala: A Python package for galactic dynamics. *The Journal of Open Source Software*, 2:388.

Schlafly, E. F., Green, G. M., Lang, D., Daylan, T., Finkbeiner, D. P., Lee, A., Meisner, A. M., Schlegel, D., and Valdes, F. (2018). The DECam Plane Survey: Optical Photometry of Two Billion Objects in the Southern Galactic Plane. , 234(2):39.

Shapley, H. (1918). Studies based on the colors and magnitudes in stellar clusters. VII. The distances, distribution in space, and dimensions of 69 globular clusters. , 48:154–181.

Simpson, J. D. (2019). The retrograde orbit of the globular cluster FSR1758 revealed with Gaia DR2. , 488(1):253–258.

Soszyński, I., Udalski, A., Szymański, M. K., Pietrukowicz, P., Mróz, P., Skowron, J., Kozłowski, S., Poleski, R., Skowron, D., Pietrzyński, G., Wyrzykowski, L., Ulaczyk, K., and Kubiak, M. (2014). Over 38000 RR Lyrae Stars in the OGLE Galactic Bulge Fields. , 64(3):177–196.

Sparke, L. S. and Gallagher, John S., I. (2007). *Galaxies in the Universe: An Introduction*.

Villanova, S., Monaco, L., O'Connell, J., Geisler, D., Minniti, D., Assmann, P., and Barba, R. (2019). Detailed chemical composition and orbit of the new globular cluster FSR1758: Implications for the accretion of the Sequoia dwarf galaxy onto the Milky Way. *arXiv e-prints*, page arXiv:1906.05653.

Wilkinson, M. I. and Evans, N. W. (1999). The present and future mass of the Milky Way halo. , 310(3):645–662.

Wu, Z.-Y., Zhou, X., Ma, J., and Du, C.-H. (2009). The orbits of open clusters in the Galaxy. , 399(4):2146–2164.

Zinn, R. (1985). The Globular Cluster System of the Galaxy. IV. The Halo and Disk Subsystems. , 293:424.

Zinn, R. (1993). The Galactic Halo Cluster Systems: Evidence for Accretion. In Smith, G. H. and Brodie, J. P., editors, *The Globular Cluster-Galaxy Connection*, volume 48 of *Astronomical Society of the Pacific Conference Series*, page 38.

Acknowledgments

Thanks to AstroMundus for providing me this precious experience to study in this program, as well as the European Union for the support of my two-year scholarship. It not only improves my academic behavior very much but also broadens my horizon and strengthen my mental toughness.

Especially, I extend thanks to University of Innsbruck in Austria for building up my solid knowledge in astronomy and astrophysics, to University of Padova in Italy and University of Belgrade in Serbia for further propelling me into professional fields of astrophysics and equipping me with practical experiences in both astrophysics and programming skills.

I would like to express my very great appreciation to Prof. Giovanni Carraro, my research supervisor, for his patient guidance, encouraging feedback and his valuable and constructive suggestions provided during the planning and development of the thesis. And thanks to my referee, Prof. Sergio Ortolani, for providing me with helpful comment on my thesis.

Special thanks to Varun M. Chaturmutha, Hitesh Lala, and Aishwarya Girdhar for giving me positive encouragement and providing me lots of helps. Thank you for always counting me in as a member of a group regarding of our nationality. Thanks for sharing me joyfulness and your delicious Indian cuisine. Remember to invite me to your wedding!

Finally, I would like to thank Wei-Cheng Lai for your psychological support and comfort whenever I felt lonely studying abroad. It is because of you that I can become better and better.